Building and Environment 293 (2026) 114365

Contents lists available at ScienceDirect

Building and Environment

journal homepage: www.elsevier.com/locate/buildenv

Understanding urban turbulence at hectometric scale using WRF-LES and eddy covariance observations

Srinidhi Gadde[a,*], Gert-Jan Steeneveld[b], Wim Timmermans[a]

[a] *Water Resources Department, Faculty ITC, University of Twente, Enschede, the Netherlands*
[b] *Meteorology and Air Quality Section, Wageningen University, Wageningen, the Netherlands*

HIGHLIGHTS

- Hectometric (100 m) WRF-LES is evaluated against urban Eddy Covariance observations.
- Performance is compared with YSU 1D PBL scheme at the same resolution.
- LES resolves turbulent structures and flux variability whereas YSU relies on parameterization.
- LES partially resolves turbulence and spectra at 50 m, while YSU produces overly smooth fluxes.

GRAPHICAL ABSTRACT

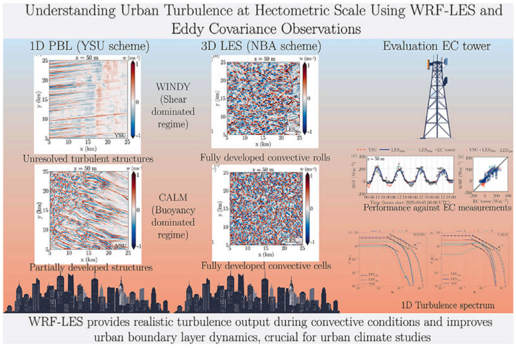

ARTICLE INFO

Keywords:
Urban
Eddy-covariance
WRF
Turbulence
Evaluation

ABSTRACT

Despite the growing application of hectometric (100-m) urban simulations, their ability to realistically represent urban turbulence remains uncertain. This study assesses the improvements offered by large eddy simulations (LES) over the commonly used Yonsei University (YSU) planetary boundary layer scheme (PBL) in urban WRF hectometric simulations at 100-m horizontal and 50-m vertical grid resolution. The results are evaluated against Eddy Covariance (EC) observations from Enschede city, The Netherlands. Two contrasting periods are examined: a windy, shear-driven event and a calm, hot, buoyancy-driven event. Both YSU and LES faithfully capture temporal patterns of near-surface meteorology. In addition, during convective conditions, LES captures realistic turbulent fluctuations indicated by turbulence spectra and resolved fluxes while YSU produces smooth fluxes. LES resolves significant portion of convective turbulence and structures (rolls during windy and cells during calm conditions), however it remains partially dependent on sub-grid scale model at first level. YSU fails to produce any convective turbulent structures during windy conditions, but succeeds in producing partially developed convective cells under calm conditions resolving upto 20% of turbulence. Partial resolving of turbulence with YSU violates the assumption of 1D PBL scheme causing potential double-counting of turbulence. Hectometric resolution is insufficient to resolve nighttime turbulence, and both schemes depend on parameterizations. The structures in LES also enhance the horizontal advection which redistributes the heat between urban and rural areas. Overall, hectometric WRF-LES generates realistic turbulence and influences boundary-layer dynamics during convective conditions, strengthening confidence in its use for urban climate studies, including heat stress assessments, and precipitation.

---

[*] Corresponding author.
Email address: s.nagaradagadde@utwente.nl (S. Gadde).

https://doi.org/10.1016/j.buildenv.2026.114365
Received 10 November 2025; Received in revised form 11 February 2026; Accepted 11 February 2026

1. Introduction

In recent years, there has been a growing shift toward using high-resolution numerical weather prediction (NWP) at sub-kilometer and hectometer (100 m) grid resolution to better represent fine-scale atmospheric processes. Hectometric simulations have improved the depiction of localized phenomena such as cold air pooling in valleys [66], tornadoes [18], and pollutant dispersion [2]. For urban applications, Ronda et al. [48] used the Weather Research and Forecasting (WRF) model [57] for fine-resolution forecasting over Amsterdam, while Forster et al. [14] applied MESO-NH to study how Paris modifies precipitation due to convection. These simulations enable capturing neighborhood-scale variability in urban morphology such as Local Climate Zones (LCZs) [59]. In urban areas with complex morphologies, quantifying energy fluxes is challenging but essential for improving forecasts and planning strategies. Previous WRF studies at grid spacings coarser than 100 m examined the urban heat island [73], and mitigation strategies [10,27,38,47,54,74].

At hectometric grid resolutions, particularly in urban environments, accurately representing land–atmosphere coupling becomes critical. Turbulence governs the vertical and horizontal exchange of momentum, heat, and moisture, thus shaping boundary-layer processes. In WRF, this coupling is typically managed using planetary boundary layer (PBL) parameterizations. These one-dimensional (1D) schemes are suitable at coarse resolutions ($\Delta x \geq 1$ km), where horizontal gradients are minimal compared to vertical gradients [34], and turbulent motions must be parameterized [21,60]. However, at hectometric grid spacings, the assumption of scale separation no longer holds. Such hectometric simulations allow for advances in including neighborhood-scale land surface temperature, urban wind and turbulence, air-quality forecasts, and convection initiation [37]. Grid spacing of 100–500 m lies in the ‘gray zone’ [70], where eddies are partly resolved and horizontal gradients become significant. Conventional 1D PBL schemes are not designed for this regime, and large-eddy simulation (LES) approaches may be more appropriate [28]. Previous WRF–LES studies over complex terrain at fine resolutions (∼10 m) have demonstrated that LES parameterization in WRF performs well in resolving large-scale turbulence and flow separation [5,55], producing results comparable to traditional computational fluid dynamics (CFD) simulations. This shows that although developed as a regional scale model, WRF has the capability to resolve turbulence. In general, LES resolves large eddies directly while modeling only subgrid-scale turbulence, thereby enhancing the fidelity of turbulence representation while reducing model dependency. However, it is worth mentioning that at hectometric resolutions while large convective eddies could be resolved, the resolution is still very coarse for nocturnal conditions [62]. Therefore, while hectometric scale simulations can be used during convective conditions they largely depend on parameterization when the turbulence scales are small during nocturnal nighttime conditions [1]. Due to this grid dependence it is necessary to study if it is feasible to use LES at these coarse resolutions, and if it provides additional resolved turbulent structures and physics. In addition, it is important to evaluate 1D PBL and 3D LES turbulence closures against observations.

In the literature, most WRF urban evaluations focus on basic meteorological variables such as temperature, humidity, and wind [9,23,50,51,71,72]. These variables largely follow the global climate model boundary forcing and are therefore less indicative of the added value of downscaling in predicting turbulent fluxes. Only a few WRF urban studies have evaluated turbulent fluxes, typically at coarse resolution ($\approx$ 1–3 km) compared to Eddy covariance (EC) observations [24,53,64]. At the microscale, very high-resolution WRF-LES studies (e.g., $\Delta x \approx 2$ m) have evaluated turbulence structure and spectra and demonstrated the benefit of multiscale downscaling for urban turbulence and dispersion [68]. However, in such comparisons WRF surface fluxes are matched against rooftop EC towers ($\approx$ 50 m above ground) using the constant-flux layer assumption [61]. With the growing use of WRF at hectometric neighborhood scales, rigorous height-consistent validation against high-quality EC tower observations becomes especially important in urban settings. However, no study has systematically examined how turbulent fluxes and associated structures vary at hectometric grid resolution in urban WRF simulations especially with LES. To address this gap, it is necessary to perform a comparative analysis of LES and a traditional 1D PBL scheme, to evaluate LES’s capability in reproducing urban fluxes and turbulence.

In this study, we evaluate whether WRF-LES at hectometric grid resolution provides a realistic representation of key urban climate variables with specific focus on turbulent sensible heat flux (SHF) compared to a 1D PBL scheme, using high-quality EC tower observations for validation. It is worth mentioning here that WRF by default only outputs surface fluxes ($z \approx 0$). Surface fluxes from WRF typically show smooth diurnal variation. However, EC measurements are carried out using masts at heights of 10’s of meters above the surface and the EC fluxes typically show more chaotic/turbulent diurnal variation with large fluctuations. In most evaluations of WRF it is assumed that the surface fluxes are equal to the atmospheric fluxes using the ‘constant flux layer’ assumption. To avoid this WRF output is extracted at appropriate model levels for height-consistent comparisons. In addition, to assess the advantages of LES over 1D PBL schemes, we investigate differences in turbulent structures, horizontal local-scale advective flux, resolved versus modeled turbulence, and the vertical variation of fluxes, providing crucial insights into surface-atmospheric coupling at hectometric grid resolution.

2. Data and methods

2.1. Observations

Continuous EC flux and meteorological quantities are being measured at the ITC International Hotel rooftop (Fig. 1(b)) in the city center of Enschede, The Netherlands (Fig. 1(a), 52.217 °N, 6.891 ° E). Enschede is a city and municipality in the province of Overijssel in the Eastern Netherlands, with a population of approximately 162,000 [6]. Enschede falls under the oceanic climate, classified as temperate oceanic climate (Cfb) according to the Köppen classification. Flux and weather measurement instruments are installed on the ITC rooftop which is approximately 46 m above the ground level, with an underlying terrain height of 38 m above MSL. Mean building height within the 500 m radius of the ITC building is approximately 17 m. The EC system at the ITC rooftop is situated at 51 m and 56 m above the ground, which is around 3 times the mean building height within the usual prescribed range of 2–5 times the mean building height [46]. Fig. 2(h) shows a panoramic view of the city center of Enschede showing the typical urban form.

Typical weather quantities such as wind direction, wind speed, air temperature, relative humidity, air pressure are measured with the Vaisala WXT520 weather transmitter [65]. Short- and long-wave up- and downwelling radiative fluxes close to the tower are measured with a Kipp & Zonen Net radiometer [3]. Three orthogonal wind components, speed of sound, and the sonic temperature are measured at a frequency of 10 Hz with a Campbell Scientific 3D-Sonic anemometer (CSAT3) complemented with LICOR 7500 openpath gas analyzer [4] (Fig. 2(b)) on a 10-meter tall mast. LI-7500 is used to measure the absolute amounts of CO_2 and H_2O at high frequency. The CSAT3 and LI-7500 together make the so-called ‘Eddy Covariance’ system used to determine the fluxes of momentum, sensible heat, latent heat, and CO_2. The CSAT3 can measure the turbulent fluctuations of horizontal and vertical wind. These measurements are then used to calculate SHF. EC observations are processed with EddyPro software and quality controlled according to Foken et al. [13]. All the above instruments combined together provides the ideal setup for evaluating the WRF model and understanding the flux dynamics in Enschede city.

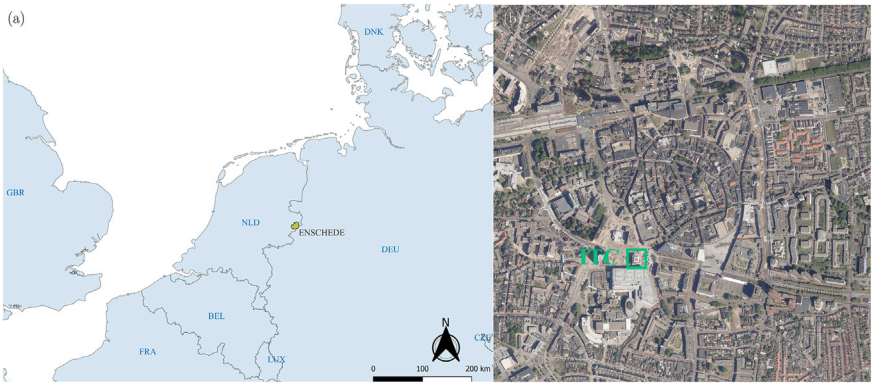

Fig. 1. (a) Map of North-Western Europe showing Enschede, and (b) Map of city center of Enschede showing the ITC rooftop where the instruments are installed.

Fig. 2. Instruments and measurement station in Enschede city. (a) 10-m tall mast over the roof, (b) CSAT3 and LI-7500, (c) RHT sensor, (d) Net radiometer setup, (e) Position of EC tower and radiation measurement setup, (f) Kipp & Zonen net radiometer, (g) Vaisala WXT520, and (h) Panoramic view of the urban form of the city center of Enschede.

2.2. WRF model setup

We use the non-hydrostatic WRF model [57] version 4.6.0, augmented with flux budget calculations using WRFlux [16]. Default outputs provided by WRF include the spatial variation of fluxes only at the surface, which does not allow for the analysis of three-dimensional (3D) variation of turbulent fluxes and mixing in the boundary layer in the vertical direction. WRFlux alleviates this problem by providing the 3D output of all the resolved and sub-grid scale turbulence components at all the levels.

WRF uses the nesting technique to scale down the phenomena from large-scale circulation toward micro-scale transport [9]. It is important to note that previously WRFlux has only been applied to idealized LES simulations without nesting. In this study, we extend its application to a real-case WRF simulation with nesting, which, to our knowledge, has not been done before. For our simulations, we use the configuration similar to Ronda et al. [48] (with additional outputs provided by WRFlux), with four one-way nested domains (Fig. 3) with the innermost domain having a grid size of 100 m. We use WRF terrain-following grids in the vertical direction, with the first atmospheric level located at a height of approximately 50 m above the ground. The coarsest domain comprises the major part of North-Western Europe as can be seen in Fig. 3(a). We employ 48 vertical terrain-following layers from the surface up to a pressure level

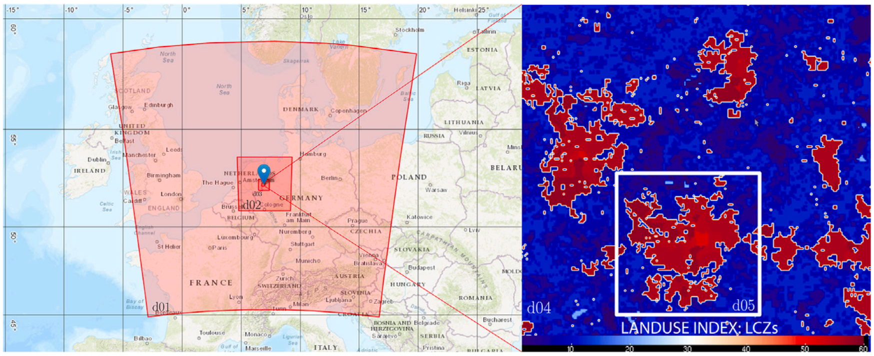

Fig. 3. (Left) Figure showing the four nested domains used in WRF simulations. (Right) Zoomed in view of the innermost domain d04 with LCZ indices. Reference fine-resolution LES domain d05 is indicated by the white square.

Table 1
Configuration of WRF simulations.

$\Delta x, \Delta y$	12,500 (d01), 2500 (d02), 500 (d03), and 100 (d04)
Δz	50 m at the first atmospheric level, stretched above
Grid points	192 × 192 (d01), 191 × 191 (d02), 191 × 191 (d03), and 301 × 301 (d04)
Reference LES $\Delta x, \Delta y$	33 m
Reference LES Δz	20 m at the first atmospheric level, stretched above
Grid points	244 × 244 (d05)
Microphysics scheme	Thompson scheme [63]
PBL scheme (d01–03)	Yonsei University Scheme [22]
Horizontal diffusion	Smagorinsky first order closure (YSU) and 3D NBA (LES)
Long-wave scheme	Rapid radiative transfer model [42]
Short-wave scheme	Rapid radiative transfer model [25]
Surface layer scheme	Revised MM5 scheme [26]
Land surface model	Noah land surface model [7]
Urban scheme	Single-layer urban canopy model (SLUCM) [35]

of 10 hPa. Table 1 provides an overview of the configuration used in our simulations.

The goal of this study is to evaluate WRF-LES at resolutions that are typically used in hectometric scale WRF studies. 50-m resolution is the default grid resolution used in WRF studies and hence we employed it in this study. The primary goal of this study is to assess whether WRF-LES, when used with default model settings typical of urban simulations, can provide performance comparable to the YSU PBL scheme while offering improvements in resolved turbulent structures. The identical vertical grid configuration was chosen to support this objective. Although LES is often conducted at finer vertical resolutions, previous studies have shown that LES can still reproduce realistic turbulence characteristics at relatively coarse vertical resolutions, particularly under convective conditions [40,43,44,62], and therefore we focus our analysis on convective conditions in the study. All the cases were run on 192 cores on the Snellius supercomputing cluster, where YSU takes approximately 64 hours of computational time while LES takes 56 hours of computational time.

In order to assess whether hectometric WRF-LES produces realistic turbulent structures and resolved scale turbulence, we also run a reference finer LES simulation (hereon $\text{LES}_{20\text{m}}$ with an additional nest d05 with a resolution of 33 m × 33 m × 20 m, respectively. For the final resolution simulation we use 60 vertical grid points uniformly distributed near the surface and stretching above.

Land-use is defined based on the hybrid dataset of Copernicus Global Land cover - MODIS - LCZ (CGLC-MODIS-LCZ) data by Demuzere et al. [12] which is available at 100 m resolution. The same dataset is used for all the domains.In the single layer urban canopy model (SLUCM), anthropogenic heat flux (AHF) of magnitude 37.5, 37.5, 12.5, 12.5, and 25 Wm^{-2} is added at the surface to LCZ2 (compact mid-rise), LCZ3 (compact low-rise), LCZ5 (open mid-rise), LCZ6 (open low-rise), and LCZ8 (large low-rise) [59] respectively. For LCZ2 this is based on the previously published estimates for Rotterdam giving a value of 37.5 Wm^{-2}, and for other LCZs default values are used. In the present study, we follow the standard practice of applying AHF as sources in SLUCM studies [35] with the default diurnal pattern provided in WRF. The default diurnal pattern for AH in WRF with hourly weights (0.16, 0.13, 0.08, 0.07, 0.08, 0.26, 0.67, 0.99, 0.89, 0.79, 0.74, 0.73, 0.75, 0.76, 0.82, 0.90, 1.00, 0.95, 0.68, 0.61, 0.53, 0.35, 0.21, 0.18) provides low weights during night time and higher values during daytime. Although prescribing anthropogenic heat adds uncertainty to absolute comparisons with EC observations, the approach is applied consistently across all simulations, ensuring that the relative comparison between PBL schemes remains robust.

The ECMWF ERA5 (European Centre for Medium-Range Weather Forecasts Reanalysis v5) data [20] was used for initial and lateral boundary conditions every hour. Furthermore, for the LES simulations following the standard procedure [15,43], we add random point perturbations with magnitude of 0.1 K to four grid points both along the lateral boundaries and vertical direction to the prognostic equations of temperature to trigger turbulence as the mesoscale forcing is not enough to trigger turbulence [45]. In idealized wall-modeled LES with periodic boundary conditions, turbulence is commonly initiated by introducing small random perturbations during model initialization [15], after which turbulence is sustained by the periodic domain configuration. In contrast, in meso-microscale coupled simulations, lateral boundary forcing derived from mesoscale or global models does not contain resolved turbulent fluctuations. As a result, it is common practice to introduce perturbations near the inflow boundaries to promote the development of turbulence within the LES domain. In our simulations, we apply small point perturbations only to the temperature field at a limited number of grid points near the lateral boundaries and within the lowest five vertical levels. These perturbations act solely as a trigger, while turbulent fluctuations in wind and other variables develop dynamically through the governing equations. Previous studies have shown that this approach produces realistic turbulence away from the lateral boundaries (see Fig. 2.6 in Muñoz-Esparza et al. [45]). To avoid the potential influence of the random perturbations, in analyzing the results, we have only sampled data away from the boundary regions and as will be shown in the results and discussion this produces realistic resolved turbulence characteristics. Consequently, the evaluation against observations is not biased by the artificial triggering mechanism. While alternative perturbation methods exist in the literature (see Muñoz-Esparza et al. [45] for a detailed comparison), the approach used here is computationally efficient, requires minimal modification to the WRF source code, and is well suited for the objectives of this study. A detailed intercomparison of different perturbation strategies is beyond the scope of the present work.

In this study, we evaluate the widely used Yonsei University (YSU) PBL scheme [22] performance against the LES results wherein the subgrid scale fluxes are modeled using 3D non-linear backscatter (3D NBA) scheme. In this study, we use the NBA model variant which is formulated exclusively in terms of the strain rates with a single model parameter, the backscatter coefficient $C_b = 0.36$. In contrast with the standard Smagorinsky sub-grid scale (SGS) model [58], NBA scheme [41] dynamically calculates the SGS momentum flux based on constitutive relations and therefore reduces the model dependency in SGS flux calculation. NBA model is better than other models available in WRF as it reproduces proper normal stresses and anisotropy due to boundary layer shear and it also incorporates backscatter of energy from SGS eddies to resolved scale eddies. In Appendix A, we give a brief description of the PBL scheme and the LES models used in the study. For evaluations, we use Root Mean Squared Error (RMSE) and Mean Bias Error (MBE) to quantify the average magnitude and direction of model errors, respectively. However, these metrics do not capture how well the model reproduces the observed variability and timing. To complement, we use Index of Agreement (IOA) [69] over R^2 because it assesses both the accuracy and precision of the model, even when the observations have low variance unlike R^2, which can be misleading in such cases. In Appendix B we provide a brief description of all the three metrics.

2.3. Turbulent flux modeling in WRF-LES

2.3.1. Surface turbulent flux calculation

Surface turbulent fluxes in WRF are modeled using the bulk aerodynamic method, which relates surface momentum flux and SHF to near-surface atmospheric conditions and surface characteristics, using,

$$\mathrm{SHF} = \rho c_p C_h |u_a| (\theta_s - \theta_a), \text{ with} \tag{1}$$

$$C_h = \frac{k^2/R}{\left[\ln\left(\frac{z}{z_{0m}}\right) - \Psi_m\left(\frac{z}{L}\right) + \Psi_m\left(\frac{z_{0m}}{L}\right)\right]\left[\ln\left(\frac{z}{z_{0t}}\right) - \Psi_h\left(\frac{z}{L}\right) + \Psi_h\left(\frac{z_{0t}}{L}\right)\right]} \tag{2}$$

where, C_h represents the surface exchange coefficient for heat, u_a is the near-surface wind speed, θ_s is the surface temperature, and θ_a is the potential temperature in the atmosphere, $R = C_d/C_h$ is the ratio of the exchange coefficients for momentum and heat, where C_d represents the surface exchange coefficient for momentum, ψ_m and ψ_h represent the stability correction functions for momentum and heat, respectively, z_{0m} and z_{0t} represent the roughness lengths for momentum and heat respectively, L is the Obukhov length, $k = 0.4$ is the von-Kármán constant. From Eq. (1) it is clear that the surface SHF is based on the difference in temperature between surface and air temperature. More details about the surface flux parameterization can be found in Chen et al. [8].

2.3.2. Atmospheric turbulent flux calculation

In contrast to surface SHF calculated using Eq. (1), the SHF at atmospheric model levels is calculated as,

$$\mathrm{SHF} = \mathrm{SHF}_{resolved} + \mathrm{SHF}_{sgs} = \left(\overline{\widetilde{w\theta}} - \overline{\tilde{w}}\overline{\tilde{\theta}}\right) - K_h \frac{\partial \tilde{\theta}}{\partial z}. \tag{3}$$

where, here K_h represents the eddy diffusivity for heat. From Eq. (1), it is evident that the surface sensible heat flux (SHF) is primarily governed by surface modeling choices. These include the land surface scheme, surface temperature, roughness lengths, and the parameterizations used to estimate the bulk heat transfer coefficient. The flux is computed using near-surface meteorological conditions, and is therefore a diagnostic output that depends heavily on how the surface–atmosphere coupling is modeled. In contrast, Eq. (3) describes the turbulent flux calculation in the atmosphere. This flux is typically derived from the resolved vertical temperature gradient and the turbulent mixing coefficients calculated by LES scheme. As such, it reflects the resolved vertical transport of heat in the atmosphere and is sensitive to the vertical structure of temperature, atmospheric stability, and turbulence represented within the model. Therefore, while surface SHF is governed by surface parameterizations, evaluating turbulent heat fluxes within the atmosphere is necessary to assess the atmospheric response and the efficiency of vertical heat transport, which cannot be inferred from surface fluxes alone.

2.4. Advective heating rate

The presence of differentially heated surfaces and hectometric-scale turbulence has been found to give rise to spatially varying thermal advective fluxes [56]. Therefore, it is necessary to quantify the contribution of local-scale horizontal advection to the variation of sensible heat flux. In this study, horizontal advective heating rate (W m^{-3}) of the sensible heat is defined as Eq. (4),

$$\mathrm{SHF}_{\mathrm{adv}} = \rho \cdot C_p \cdot \left(\bar{u} \cdot \frac{\partial \bar{\theta}}{\partial x} + \bar{v} \cdot \frac{\partial \bar{\theta}}{\partial y}\right) \tag{4}$$

in which ρ is the density of air ($\mathrm{kg\,m^{-3}}$), and C_p is the specific heat capacity of air at constant pressure ($\mathrm{J\,kg^{-1}\,K^{-1}}$), $\bar{\theta}$ is the temperature in K, and $\bar{u}$ and $\bar{v}$ are the horizontal winds in the x and y directions, respectively. All the terms are half-hourly averaged. All the advection terms are calculated at the mass points in the WRF Arakawa C-grid.

2.5. Numerical experiments and synoptic conditions

In this study, we consider two contrasting events with high wind speed in April, 2020 and calm, low wind speed event in August, 2020. The two contrasting cloud-free, turbulent events in April and August are based on wind speed and convection which are detailed in the Sections 4.1 and 4.2. For both events, we perform two simulations with, (a) YSU PBL scheme (Appendix A) (hereon YSU) and (b) NBA model with Smagorinsky scheme with LES (Appendix A) (hereon $\mathrm{LES_{50m}}$). The reference LES with finer resolution is indicated as $\mathrm{LES_{20m}}$. For the Windy event, we perform the simulations from 2020-04-18 00:00 UTC to 2020-04-23 00:00 UTC (hereon ‘windy’ event), where the first day of the simulations (2020-04-18) is considered as spinup. Similarly, for the Calm event, we perform the simulations from 2020-08-04 00:00 UTC to 2020-08-09 00:00 UTC (hereon ‘calm’ event), where the first day of the simulations (2020-08-04) is considered as spinup. We only consider the last four days of the simulations for evaluation.

The clear sky days chosen for the study are based on the hourly cloud cover data from the nearest meteorological station at Twente Airport (52.273 N, 6.891 E) maintained by the Royal Netherlands Meteorological Institute, KNMI (Koninklijk Nederlands Meteorologisch Instituut). In the hourly data from KNMI the cloud cover measured with a ceilometer [32] is provided in oktas (eighths) from 0 (completely cloudless) to 8 (completely cloudy). First, we identified all the cloud free days in 2020 (oktas = 0) and identified continuous cloud free days of at least four days length. The clear-sky days were chosen to make sure that there is a pronounced diurnal cycle and there is little influence of clouds on the fluxes. Furthermore, simulating full diurnal cycle would facilitate the analysis in both stable and unstable conditions.

2.5.1. Case 1: Windy event, 18–22 April, 2020

During this event, Enschede city was situated at the edge of a high pressure system (Fig. 4(a)), with a steep pressure gradient causing high wind speeds in the region. Near surface air temperature was moderate varying between 5–20 ° C. The pressure gradient gave rise to mostly Easterly wind in the region with high wind speeds (4–8 $\mathrm{ms^{-1}}$ at 10 m height, Fig. 4(b)).

2.5.2. Case 2: Calm event, 04–08 August, 2020

During this event, Enschede city was situated at the edge of an Icelandic low, a high over Eastern Europe, and a low over Southern Europe (Fig. 4(c)). The high pressure system gradually strengthened over

(a) Geopotential height at 500 hPa for 2020-04-20UTC12:00:00 (b) Wind Rose - 2020-04-19 to 2020-04-23

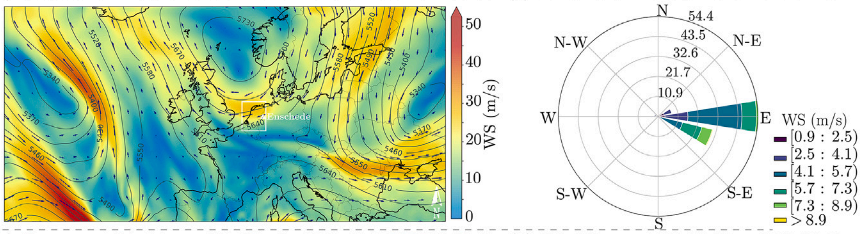

(c) Geopotential height at 500 hPa for 2020-08-06UTC12:00:00 (d) Wind Rose - 2020-08-05 to 2020-08-09

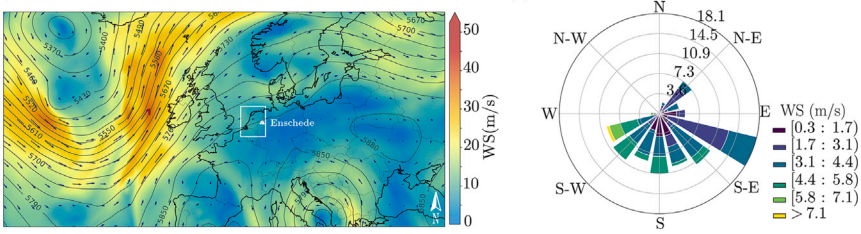

Fig. 4. Synoptic chart of geopotential height at 500 hPa superimposed on wind speed map on (a) Windy event (2020-04-20) and (b) Calm event (2020-08-06). Enschede is marked with a triangle and Netherlands is highlighted with the black rectangle. Arrows indicate the wind speed vectors, the contour lines indicate the geopotential height in meter.

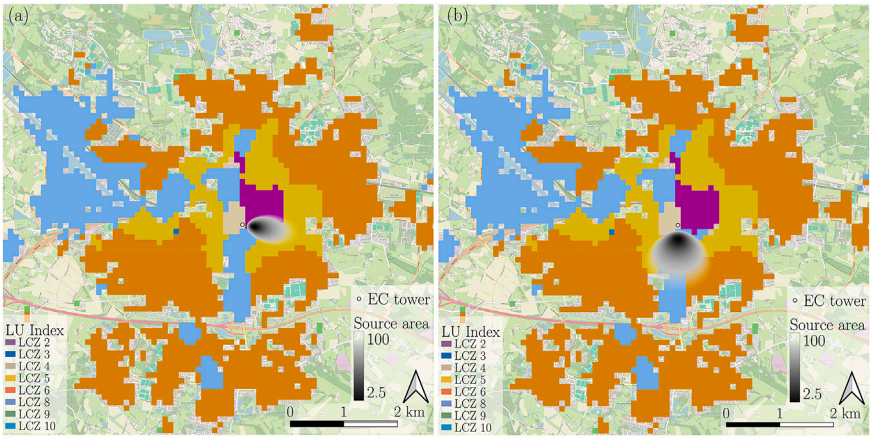

Fig. 5. Maps showing local climate zones (LCZs), location of the EC tower, and source area footprint for the fluxes in (a) Windy event at 1200 hours on 2020-04-20 and (b) Calm event at 1200 hours on 2020-08-06. In Fig. 5 the EC tower location is marked with a circle. For brevity, we only show the urban land cover types. Cumulative contribution of the footprint to the total flux is shown by the color gradient, with darker shades indicating larger contribution to the footprint.

the course of next two days, with whole of Europe in a high pressure system, yielding a stable, low wind speed, warm episode. Enschede over the course of 4 days experienced mostly Southerly winds (mostly 0–3 ms^{-1} at 10 m height, Fig. 4(d)). This calm event involved high land-surface heating with air temperature reaching 30 ° C [31].

2.6. Source area footprint modeling

While radiative fluxes are primarily local in nature being governed by the immediate surface characteristics and atmospheric conditions directly above, the turbulent fluxes measured by the EC systems are influenced by conditions over a broader upwind area. In boundary-layer meteorology, it is common practice to apply a footprint model to relate the turbulent fluxes observed at a certain height to the area at which corresponding surface exchange processes occur. This approach accounts for the fact that advective transport integrates information from a spatially distributed source area, rather than from a single point. For comparing the surface fluxes from WRF against EC measurements a weighted average of the surface fluxes over a footprint is performed. In this study, we use the Urban Multi-scale Environmental Predictor (UMEP) plugin [39] in QGIS to calculate the source area footprint.

During the windy event (Fig. 5(a)) the footprint is elongated and shifts Eastward, consistent with the dominant Easterly winds. It spans a heterogeneous mix of LCZ types, including compact mid-rise (LCZ 2), open mid-rise (LCZ 5), large low-rise (LCZ 8), and open low-rise (LCZ 6). According to the footprint model, cumulatively LCZ 2 and LCZ 8 contribute up to 75% of the fluxes measured at the EC tower. Cumulative contribution indicates the percentage contribution of each LCZ to the total flux. With the UMEP plugin we produce maps of weights for each footprint. Enschede is mostly urban with sparse vegetation, and therefore default LCZs accurately represent the dominant land use.

In contrast, during the calm event (Fig. 5(b)) footprint is more circular, reflecting weaker directional wind and enhanced convective mixing. The footprint is mostly constrained to LCZ 8 and LCZ 5. Shape of the footprint gives a clue as to dominance of shear or convective turbulent mixing in the atmosphere. The footprints shown in Fig. 5(a) and (b) are used for obtaining weighted average of the WRF surface fluxes for evaluation.

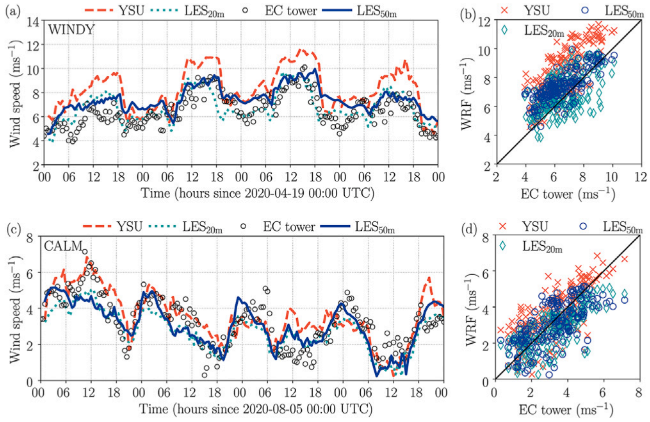

Fig. 6. Time series and scatter plot of modeled and observed wind speed (a,b) Windy event and (c,d) Calm event.

Table 2
Statistical metrics comparing wind speed from WRF against observations.

Event	Case	R^2	IOA	RMSE (ms^{-1})	MBE (ms^{-1})
Windy	YSU	0.56	0.42	2.08	1.73
Windy	LES_{50m}	0.61	0.53	1.22	0.89
Windy	LES_{20m}	0.35	0.56	1.21	0.15
Calm	YSU	0.53	0.59	1.13	0.47
Calm	LES_{50m}	0.45	0.59	1.07	0.02
Calm	LES_{20m}	0.57	0.61	1.01	-0.46

3. Results

3.1. Wind speed

The time series of wind speed (Fig. 6(a), c) for both the windy and calm events shows that both schemes reproduce the overall temporal evolution, though differences appear in their ability to capture observed variability. During the windy event, LES follows the observed wind speed more closely, while YSU tends to slightly overestimate values between 10:00 and 18:00 UTC. In the calm event, both schemes show comparable behavior, tracking the observed diurnal cycle with similar fidelity.

Scatter plots (Fig. 6(b), d) highlight these contrasts. For the windy event, LES_{50m} shows a tighter clustering around the 1:1 line with lower dispersion compared to YSU, indicating a closer match to observations under convective conditions. LES_{20m} shows more variability compared to LES_{50m} as more turbulence is resolved and the results are more fluctuating. For the calm event, both models reproduce the variability reasonably well, though LES displays somewhat reduced scatter and a smaller mean error. These visual assessments are supported by the statistical metrics summarized in Table 2. In the windy case, LES_{50m} yields lower RMSE (1.23 ms^{-1}) and MBE (0.89 ms^{-1}) compared to YSU (RMSE = 2.08 ms^{-1}, MBE = 1.73 ms^{-1}), along with a higher IOA (0.53 vs. 0.42). Compared with LES_{20m}, hectometric LES_{50m} shows similar performance. In the calm case, both YSU and LES_{50m} achieve similar IOA (≈ 0.6).

Overall, both schemes are able to capture the main temporal features of the observed wind speed. LES shows a slightly better agreement with observations, particularly during the windy event, whereas YSU shows a slight overestimation during peak solar heating. These results suggest that LES successfully predicts the temporal dynamics of wind speed under convective conditions, while both approaches perform comparably during the calm event.

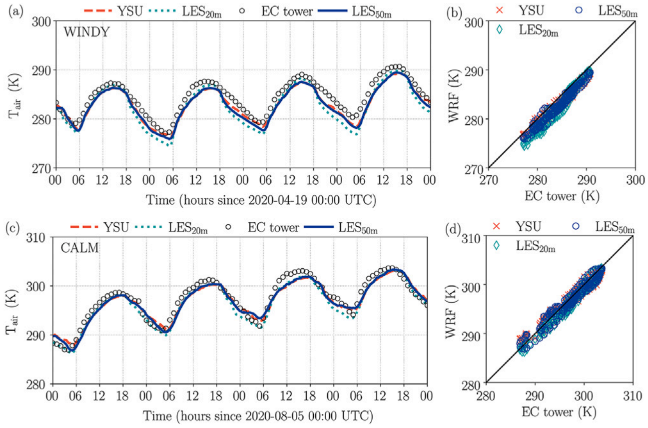

Fig. 7. Time series and scatter plot of modelled and observed air temperature for (a,b) Windy event and (c,d) Calm event.

Table 3
Statistical metrics comparing air temperature (T_{air} (K)) from WRF against observations.

Event	Case	R^2	IOA	RMSE (K)	MBE (K)
Windy	YSU	0.97	0.76	1.52	−1.38
Windy	LES_{50m}	0.97	0.75	1.66	−1.54
Windy	LES_{20m}	0.95	0.73	2.10	−1.84
Calm	YSU	0.98	0.89	0.86	−0.22
Calm	LES_{50m}	0.97	0.90	0.85	−0.23
Calm	LES_{20m}	0.97	0.89	1.08	−0.70

3.2. Temperature

The time series of air temperature (Fig. 7(a), c) show that both schemes reproduce the observed diurnal cycle well. During the windy event, both YSU and LES slightly underestimate daytime peaks, while during the calm event, simulated temperatures track observations closely with only a small negative (cold) bias.

In our simulations, we employ SLUCM, in which AH fluxes are prescribed *a priori* based on LCZ-dependent values rather than being dynamically calculated by a building energy model. Consequently, our configuration does not include dynamically calculated internally generated, time-varying building waste heat, and air conditioning as would occur in a coupled building energy parameterizations (BEP) but neglects all other sources of AH. Instead, the imposed AH acts as an additional grid-cell averaged sensible heat source. During daytime, its magnitude (12.5–38 Wm^{-2}, depending on LCZ) remains modest relative to net radiative fluxes and therefore does not dominate the surface energy balance. This is consistent with the persistence of a cold bias in near-surface air temperature, indicating that other processes (for example, surface radiative properties and energy partitioning) exert stronger control on the modeled thermal state. During nighttime, AH fluxes are still applied following the prescribed diurnal profile; however, their magnitude is substantially smaller (approximately 3–10 Wm^{-2}). While this additional heat source leads to weakly positive sensible heat fluxes over some urban surfaces, it is not sufficient to offset the modeled cold bias. We therefore hypothesize that the nighttime cold bias is more strongly linked to enhanced longwave radiative cooling, potentially associated with uncertainties in prescribed surface emissivity or radiative parameterization. A dedicated sensitivity analysis of these effects is beyond the scope of the present study.

The scatter plots (Fig. 7(b), d) further confirm this close correspondence, with strong correlations between modeled and observed values. The windy event simulations show a somewhat wider spread, consistent with the higher RMSE values reported in Table 3. Statistical

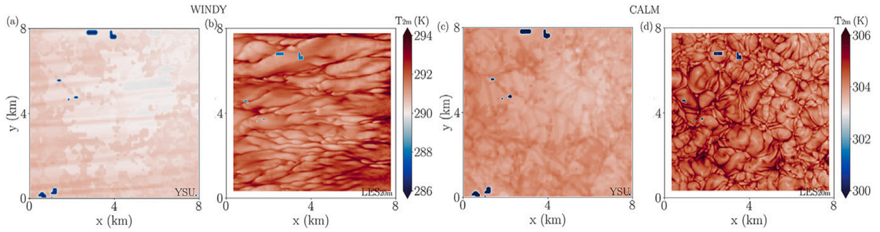

Fig. 8. Spatial variation of 2-m air temperature (a,b) Windy event at 2020-04-22 12:00 UTC and (c,d) Calm event at 2020-08-08 12:00 UTC.

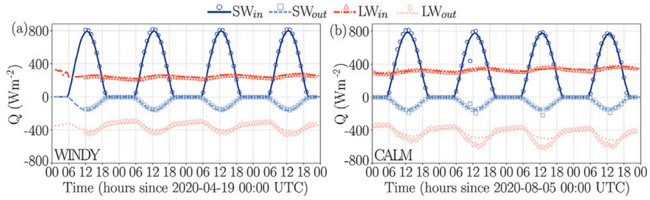

Fig. 9. Radiation components including incoming and outgoing shortwave (SW_{in}, SW_{out}) and longwave (LW_{in}, LW_{out}) radiation for, (a) Windy event, (b) Calm event. Lines represent WRF results and markers represents EC tower observations.

metrics (Table 3) indicate nearly identical performance between the two schemes. Both YSU and LES achieve high R^2 across both events, demonstrating that WRF captures the temporal variability well. IOA values are also high (0.75–0.85), particularly in the calm case. RMSE remains around 1 K for the calm event and around 1.5–2 K for the windy event. Both schemes show a consistent small cold bias (MBE between -0.2 and -1.5 K). LES_{20m} shows higher bias compared to other simulations as this simulation resolves more turbulence than LES_{50m} thereby producing more fluctuations and hence higher spread in the data. Fig. 8 supports this argument as it shows that with LES_{20m} there are turbulent structures that are observed while such pronounced structures are not dominant in the YSU results. This indicates differences in spatial distribution of air temperature at the neighborhood scale based on the local flow structures. Details of turbulent structures under two conditions will be discussed in detail in Section 4.1.

Overall, LES and YSU yield very similar performance in reproducing observed air temperature at the EC tower height. Both schemes reliably capture the diurnal cycle and variability, with improved agreement during the calm case. The minor systematic cold bias is consistent across schemes and likely reflects differences in surface representation rather than the turbulence parameterization itself. Since resolving or correcting such biases is outside the scope of this work, we focus instead on the comparative behavior of LES and YSU in representing turbulent fluxes and vertical variability.

3.3. Radiative fluxes

In Fig. 9(a) and (b) radiative fluxes from only LES simulations are presented in the figure as there was negligible difference between LES and PBL runs. Incoming solar radiation is correctly predicted for both windy and calm events (Fig. 9(a) and (b)). As we chose cloud-free days for the evaluations, the incoming solar radiation shows a clear diurnal cycle with the maximum value of approximately 800 Wm^{-2}. WRF slightly underestimates the SW_{in} with an MBE of -2.3 Wm^{-2}, and an RMSE of 26.9 Wm^{-2}. Ruiz-Arias et al. [49] in their intercomparison study of different radiation models in WRF report a similar negative bias in irradiance values with the RRTMG model, which is attributed to the differences in the aerosol concentration.

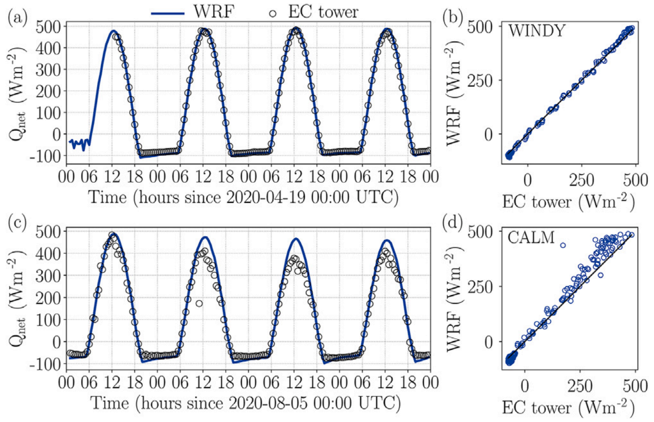

Fig. 10. Net radiation during (a) Windy event and (b) Calm event. Lines are from WRF results, markers represent EC tower observations.

LW_{in} during the windy event has an average value of 251 Wm^{-2}, and during the calm event has an average value of 329 Wm^{-2}. LW_{in} shows less pronounced diurnal variation but reflects seasonal differences in atmospheric temperatures. WRF predicts LW_{in} very well, with an MBE of 4.2 Wm^{-2} and RMSE of 10.7 Wm^{-2}. LW_{out} shows a diurnal cycle with maximum values around the solar peak with the values being lower during Windy event compared to Calm event.

It is important to note that while radiation measurements from the observational site represent point-scale conditions, WRF outputs represent fluxes on a 100-m grid. As a result, direct comparisons particularly of upwelling fluxes which are highly sensitive to local surface properties should be interpreted with caution. For the chosen roof albedo of 0.3 and emissivity of 0.98 in WRF, upwelling fluxes SW_{out} and LW_{out} match reasonably well with the observations.

As the individual radiation components are rather well predicted, Fig. 10(a, b) where the net radiation is calculated as $SW_{in} - SW_{out} + LW_{in} - LW_{out}$ is also well predicted. Observations for the first half of the day on 2020-04-19 were missing and therefore not plotted in Fig. 10(a). The figure shows that for both the events WRF results match well with the observations even though there is a mismatch in the scales. For both the events we observe a peak net radiation approximately at 450–500 Wm^{-2} and reliable diurnal variations. For the windy event, RMSE and MBE are 10.45 and -1.89 Wm^{-2}, respectively. For the calm event, RMSE and MBE are 42.15 and 14.88 Wm^{-2}, respectively. These results provide confidence in the model's ability to simulate surface radiative forcing, which is a critical driver for surface energy partitioning and boundary-layer development in urban environments.

Overall, the WRF-LES realistically reproduces the magnitude and timing of surface radiative fluxes for both seasons. The amplitude, phase, and temporal variability of the modeled radiation terms are consistent with expected physical behavior and observational studies. Minor discrepancies may arise from simplifications in the land surface or

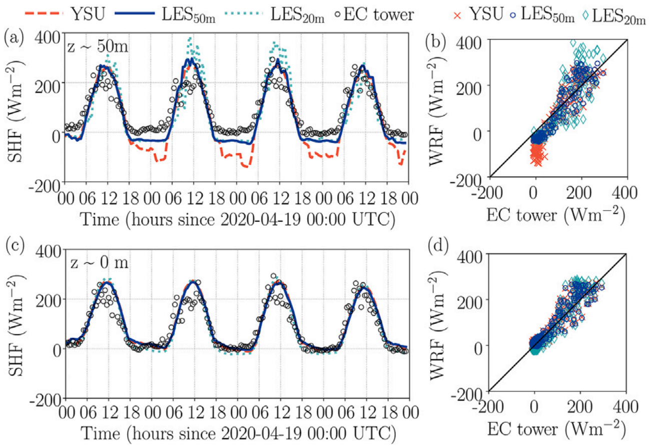

Fig. 11. Comparison of time series and scatter plot of modeled and observed SHF against observations for windy event at (a,b) Observation height (c,d) Surface.

radiation schemes and differences in the scale of measurements but do not substantially affect the overall energy balance.

3.4. Evaluation of SHF and 'constant flux layer' assumption

3.4.1. Windy event

During the windy event, both surface and 50-m fluxes display a clear diurnal cycle, with daytime peaks above 200 Wm^{-2} (Fig. 11). At the surface (Fig. 11c), WRF reproduces this diurnal evolution well, with only small differences between YSU and LES. At 50 m, both schemes follow the daytime cycle reasonably, but differences emerge at night. YSU produces unrealistically strong negative fluxes (≈ -125 Wm^{-2}), whereas LES predicts a weakly stable boundary layer with smaller negative values (≈ -30 Wm^{-2}). Large negative fluxes with YSU are consistent with its nonlocal formulation, which prescribes a vertical profile of eddy diffusivity and likely maintains excessively large diffusivity values at 50 m under stable conditions, thereby enhancing downward heat transport beyond what would be expected at that height. In addition, YSU model is developed for resolutions much coarser than 100-m, so the applicability of YSU at hectometric resolutions remains uncertain. It is worth mentioning here that due to the diurnal profile applied in WRF maximum AH during night does not exceed 10 Wm^{-2} and therefore is not strong enough to produce large negative fluxes observed with YSU model.

It is worth mentioning here that at nighttime, hectometric resolution LES does not resolve any turbulent structures as stable boundary layers require a finer grid resolution [1] and therefore it is fully dependent on SGS modeling. In our results, LES performs better during nighttime, as the SGS model performs better when compared to YSU model and this difference in performance is not related to the resolved turbulence.

Observed fluxes from the EC tower remain slightly positive at night, reflecting near-neutral conditions that neither scheme fully captures. This contrast arises because WRF's surface SHF includes anthropogenic contributions in the SLUCM energy balance, keeping nighttime values slightly positive, while fluxes at 50 m (diagnosed using Eq. (3)) depend directly on the resolved vertical temperature gradient. As a result, 50-m fluxes are more sensitive to how well surface–atmosphere coupling is represented. Both schemes capture daytime coupling well, but nighttime behavior diverges, illustrating that while a constant-flux layer may still exist under stable conditions, it becomes much shallower and is therefore not resolved at the current vertical resolution. Consequently, the 'constant flux layer' assumption holds during convective periods but becomes less applicable at 50 m under stable conditions.

Scatter plots (Fig. 11(b), d) highlight these differences: WRF reproduces the overall variability, though YSU produces excessively negative values at night. Table 4 confirms that both schemes perform similarly at the surface and 50 m. Overall, both approaches capture the daytime SHF evolution during the windy event. As explained in the introduction, during nighttime hectometric resolution is not sufficient to resolve turbulence and therefore the comparison in Table 4 is between SGS parameterization. We explain this in detail in Section 4.3. While daytime agreement between observations and simulations is reasonable, during nighttime YSU shows a high RMSE at 50-m height indicating a non-physical boundary-layer cooling. Our objective here is not to resolve or correct the nighttime biases in SHF, but rather to assess how LES compares with a traditional PBL scheme in representing turbulent fluxes and surface–atmosphere coupling.

Table 4
Statistical metrics comparing SHF from WRF against observations during convective (06:00–18:00 hours) and stable conditions (00:00–06:00 or 18:00–00:00 hours), respectively. A vertical line separates the statistics corresponding to the two conditions. All fluxes are footprint averaged.

Event	Height (m)	Case	R^2	IOA	RMSE (Wm^{-2})	MBE (Wm^{-2})
Windy	0	YSU	0.66|0.44	0.67|0.57	47.45|15.61	21.41|−0.92
Windy	0	LES$_{50m}$	0.65|0.46	0.68|0.53	45.50|15.71	17.11|3.94
Windy	0	LES$_{20m}$	0.70|0.58	0.70|0.52	48.71|21.00	16.29|−16.07
Windy	50	YSU	0.66|0.43	0.69|0.16	48.43|85.92	7.78|−79.94
Windy	50	LES$_{50m}$	0.68|0.64	0.67|0.27	50.99|43.37	9.37|−41.50
Windy	50	LES$_{20m}$	0.51|0.61	0.56|0.29	79.72|40.28	10.26|−38.17
Calm	0	YSU	0.47|0.13	0.58|0.29	49.91|49.54	13.53|43.31
Calm	0	LES$_{50m}$	0.48|0.19	0.58|0.29	48.99|49.03	10.51|43.26
Calm	0	LES$_{20m}$	0.51|0.21	0.62|0.39	47.35|33.68	8.35|24.86
Calm	50	YSU	0.48|0.10	0.62|0.38	50.33|36.63	11.88|−6.29
Calm	50	LES$_{50m}$	0.47|0.33	0.63|0.49	49.48|23.79	−0.41|−1.98
Calm	50	LES$_{20m}$	0.38|0.26	0.61|0.40	57.31|25.12	2.97|1.46

3.4.2. Calm event

The time series of SHF for the calm event (Fig. 12a, c) shows lower daytime peaks compared to the windy event, with EC observations reaching maxima of 100–150 Wm^{-2} at peak solar heating, despite 2-m air temperatures around 30 °C. Nighttime SHF is negative (≈ -30 Wm^{-2}), indicating a stable boundary layer (SBL), in contrast to the near-neutral nights in April. This difference is consistent with lower nighttime wind speeds and stronger radiative cooling during the calm event.

At the surface (Fig. 12(c), WRF overestimates daytime SHF and does not reproduce the observed nighttime negative flux, likely because SLUCM adds anthropogenic heat flux to the surface balance. At 50 m, LES better represents the nighttime SBL, while YSU produces excessively negative SHF (-100 Wm^{-2}) during the first two nights. During daytime, both schemes overestimate SHF, but the diurnal cycle is still well captured. Scatter plots (Fig. 12b, d) and metrics in Table 4 confirm these results with both YSU and LES performing well during daytime conditions. Similar to the Windy event, WRF surface fluxes can be used to compare against the EC observations during daytime under the 'constant flux layer' assumption for both YSU and LES, while such a comparison can only be made with LES during nighttime due to the shallow nature of the surface layer in stable boundary layers.

Overall, both WRF-LES and YSU reproduce the observed SHF reasonably well, though nighttime SBL representation remains a challenge. LES simulates negative fluxes at night more consistently, while YSU tends to exaggerate stability. However, better performance of LES is not related to the turbulence being resolved but rather to better SGS parameterization compared to YSU. For LES, the hectometer resolution is insufficient to resolve the nocturnal turbulence which would require very high grid resolutions [1]. Despite warmer conditions in August, SHF values are lower than in April, underscoring the key role of turbulent momentum exchange in regulating surface–atmosphere coupling. At the surface, differences between the schemes remain small because fluxes are strongly constrained by the land surface parameterization. However, at the observationally consistent height of 50 m, differences become more apparent, highlighting the sensitivity of surface–atmosphere coupling to

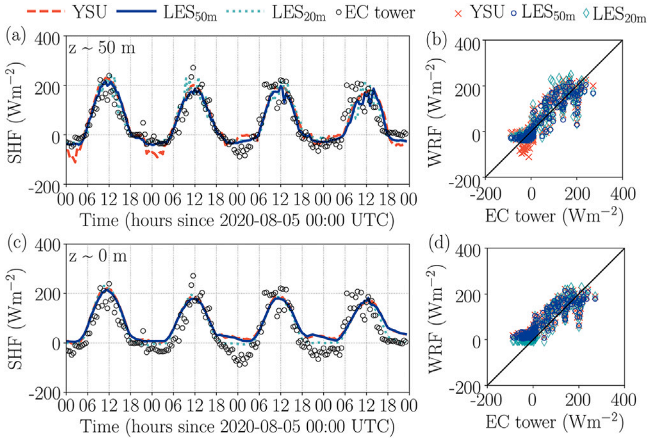

Fig. 12. Comparison of time series and scatter plot of modeled and observed SHF against observations for calm event at (a,b) Observation height (c,d) Surface. All fluxes are footprint-averaged.

turbulence representation. These evaluations show that LES and YSU provide broadly comparable performance for basic meteorological variables and near-surface fluxes, supporting the use of WRF-LES for urban simulations at hectometric resolution. A key advantage of LES is its ability to resolve turbulent structures and influence spatial organization of turbulent fluxes during convective conditions. In the following discussion, we focus on how differences in turbulent structures and advective fluxes emerge between YSU and LES.

4. Discussion

4.1. Turbulent structures and horizontal local-scale advective fluxes in urban areas

The organization of horizontal advective fluxes within urban areas is closely tied to the underlying turbulent structures, as these control the spatial distribution of wind and temperature gradients. We therefore begin by analyzing vertical velocity fields to characterize turbulence in the two events. We note here that this analysis is limited to the daytime convective conditions. The relative role of mechanical turbulence (wind shear) during the windy event and buoyant turbulence (surface heating) during the calm event can be characterized by the ratio z_i/L, where z_i is the PBL height and L is the Obukhov length. Previous studies [17,52,67] show that for $-z_i/L \approx$ 15–20, turbulent exchange is dominated by convective rolls, while for $-z_i/L > 25$, the system transitions to convective cells, with buoyancy-driven turbulence dominating. In our simulations, $-z_i/L < 10$ for the windy event and $-z_i/L > 100$ for the calm event at peak solar heating. Consistent with theory and observations [11,17,30,52,67], LES reproduces quasi-two-dimensional streamwise convective rolls during the windy case (Fig. 13b) and cellular convection under buoyancy-dominated conditions in the calm case (Fig. 13f). In order to ensure that the structures observed in hectometric $\text{LES}_{50\text{m}}$ are not just numerical artifacts, we also present the turbulent structures from fine resolution $\text{LES}_{20\text{m}}$ at two heights 20 m and 60 m (Fig. 13). The figures show that hectometric $\text{LES}_{50\text{m}}$ (Fig. 13(b, f)) produces realistic turbulent convective rolls and cells very similar to high-resolution $\text{LES}_{20\text{m}}$ (Fig. 13(c, d, g, h)).

YSU scheme does not produce fully developed coherent turbulent structures in either case. During the windy event, only weak mesoscale perturbations appear (Fig. 13(a), while in the calm event the simulated structures are poorly developed and would require longer fetch to organize into resolved convection (Fig. 13(e); [45]). These differences align with the stronger winds in April versus the weak winds in August. The turbulent structures captured by LES confirm that WRF-LES at hectometric resolution can realistically reproduce convective turbulence in urban boundary layers, while the YSU scheme remains limited by its 1D formulation. It is worth mentioning that, at hectometric resolution, the YSU scheme manages to resolve a few turbulent structures during the calm event. However, this is counterproductive, as it leads to partial resolution of turbulence, which violates the assumptions of the PBL scheme that grid scale turbulence is negligible. This potentially leads to double counting of turbulence which will be made clear in the upcoming section dealing with the partitioning of resolved and SGS fluxes.

The difference in turbulence structures between the two simulations is also reflected in the one-dimensional velocity spectra (Fig. 14). These spectra are plotted for the hours 10:00 to 14:00 UTC on 2020-04-19 and 2020-08-05, respectively. The $\text{LES}_{50\text{m}}$ runs suggest the characteristic form of the ABL spectra, with an inertial subrange that follows the Kolmogorov $-5/3$ scaling, as well as the expected anisotropy between the longitudinal and transverse velocity components. Toward smaller scales (large wavenumbers), the v and w spectra converge, reflecting the transition toward local isotropy in the inertial subrange (consistent with Figure 2 in Kaimal and Finnigan [29]). The collapse of v and w energy at high wavenumbers, together with the steeper decay of the u spectrum, indicates that the LES is resolving a portion of the turbulent cascade down to the grid scale. As expected, the finer-resolution $\text{LES}_{20\text{m}}$ resolves a larger fraction of turbulent energy than $\text{LES}_{50\text{m}}$. The comparison between these two LES configurations also indicates that hectometric LES does not fully resolve the turbulence spectrum but

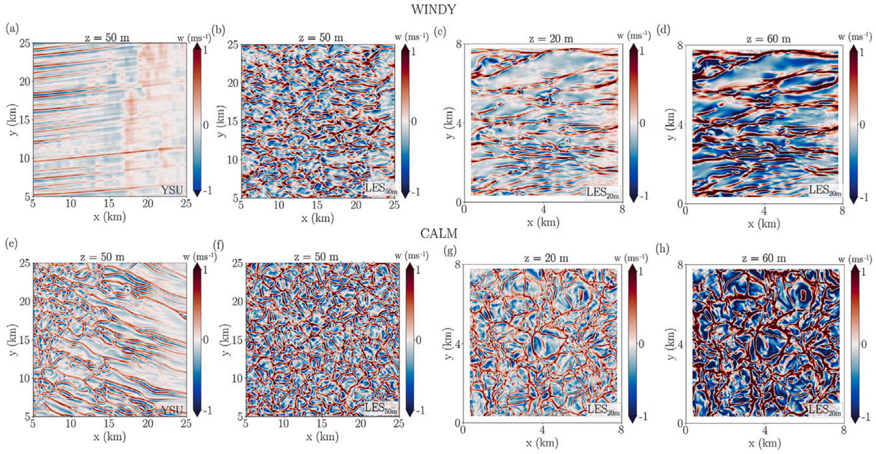

Fig. 13. Horizontal cross-section of vertical velocity for (a,b,c,d) Windy event (on 2020-04-22 12:00 UTC) and (e,f,g,h) Calm event (on 2020-08-08 12:00UTC), for YSU, $\text{LES}_{50\text{m}}$, and $\text{LES}_{20\text{m}}$, respectively.

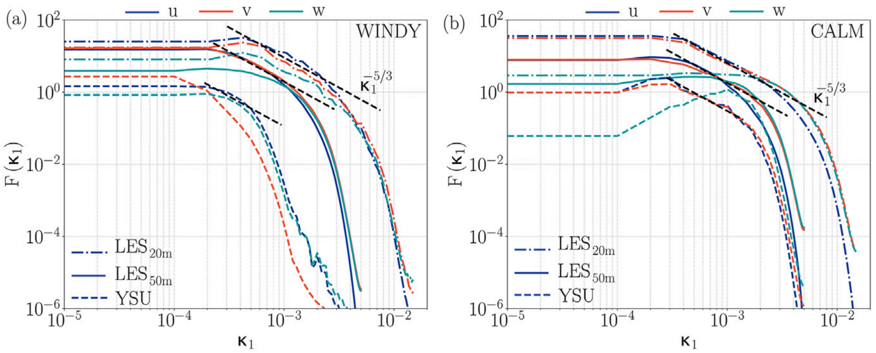

Fig. 14. One-dimensional velocity spectra during convective conditions for (a) Windy day (2020-04-19 10:00-14:00 UTC), and (b) Calm day (2020-08-05 10:00-14:00 UTC).

captures a dynamically consistent portion of the energy-containing and inertial subrange motions under convective conditions. In relative terms, LES_{50m} resolves substantially more turbulent energy and preserves more realistic spectral structure than the YSU simulation.

In contrast, the YSU spectra show a more rapid decay of energy with wavenumber, indicative of limited representation of smaller-scale turbulent motions and a more diffusive effective behavior of the closure at this resolution. The YSU spectra also do not consistently exhibit the expected transition from anisotropy at large scales to greater isotropy at smaller scales. For example, in the windy case, the transverse velocity component departs from the $-5/3$ behavior, while in the calm, buoyancy-dominated case, the vertical velocity spectrum contains substantially less energy than in LES, suggesting weaker representation of buoyancy-driven motions. Specifically, in the calm case, the LES w-spectral energy at the energy-containing scales is on the order of 10^{0}, whereas the YSU w-spectral energy is on the order of 10^{-2}, corresponding to a difference of $\mathcal{O}(10^{2})$ (approximately two orders of magnitude).

These differences indicate that, although some variability becomes resolved at hectometric resolution, the turbulence cascade is only partially represented in the YSU simulation. At grid spacings of $\mathcal{O}(100\,\mathrm{m})$, the model operates in the so-called *gray zone* (or *terra incognita*) of boundary-layer modeling [70], where energy-containing turbulent motions begin to be partially resolved while parameterizations are still formulated under the assumption that turbulence is predominantly subgrid. Because 1D PBL schemes such as YSU are not scale-aware, they do not adjust parameterized mixing in response to resolved turbulent motions, which can lead to an inconsistent partitioning between resolved and parameterized transport.

Overall, while 100-m resolution does not capture the smallest turbulent scales, the LES simulations reproduce spectral characteristics that are more consistent with canonical ABL turbulence behavior, whereas the YSU closure yields a more weakly energetic and less dynamically structured turbulence field. These differences in the distribution of turbulent energy across scales contribute to differences in the role of advection in the simulated energy balance.

Differences in turbulent structure directly shape horizontal advective heating rates over urban pixels (Fig. 15c, d, g, h). In LES, fluxes show clear roll- and cell-like organization, while in YSU they remain weak. The magnitudes of SHF_{adv} in LES are consistently many times larger than in YSU, underscoring the role of resolved turbulence in enhancing lateral heat transport across the urban canopy layer. We note that LES flux magnitudes can be sensitive to resolution, particularly when simulations operate near the energy-containing scales without fully resolving the inertial and dissipation ranges. However, the finer-resolution LES_{20m} simulation, performed with identical forcing, exhibits similar turbulent organization and even stronger relative advective heating rates. This suggests that the enhanced horizontal advection in LES is not solely a consequence of marginal resolution, although the absolute magnitude of advective fluxes may remain resolution-dependent. During the windy event, advective fluxes are dominated by the streamwise component, reflecting the easterly wind and roll alignment, while in the calm case both streamwise and crosswind contributions are comparable, consistent with cellular convection. Although not generalizable without sensitivity tests, the urban signal shows a distinct contrast: positive SHF_{adv} during the windy spring event, and negative SHF_{adv} during the calm summer event. As expected LES_{20m} due to higher resolution and turbulence, shows higher advective heating rate when compared to LES_{50m}. Complete physical interpretation is outside the scope of the current study, however the structural organization and stronger magnitudes are robust LES features, further justified by the high resolution LES. A full sensitivity analysis of the urban warming or cooling through, advection is beyond the scope of the present study. The results indicate that the resolved turbulent structures give rise to neighborhood-scale energy transport in urban areas. The ability of hectometric simulations to resolve horizontal advection has been previously reported in Simó et al. [56]. Furthermore, WRF simulations at 1 km resolution also underline the importance of advection in heat transport in urban areas [19].

4.2. Horizontal and vertical advective flux divergence over urban areas

The vertical profiles of horizontal advective heating rate averaged over urban pixels surrounding Enschede, $\langle SHF_{adv}\rangle$ (Fig. 16(a)–d) ($\langle\rangle$ represents planar averaging), show that in both events LES produces larger near-surface magnitudes than YSU. During the windy event, $\langle SHF_{adv}\rangle$ is positive at the first model level close to the urban surfaces, a signature of streamwise roll organization that channels heat laterally across the urban boundary layer (Fig. 13(d). In contrast, during the calm event, near-surface $\langle SHF_{adv}\rangle$ is negative, reflecting the divergent transport associated with cellular convection (Fig. 13(h). In both cases, LES enhances lateral energy transport in the urban atmosphere compared to YSU, underscoring the importance of explicitly resolved turbulence for neighborhood-scale urban–atmosphere coupling. However, it is worth emphasizing here that while LES_{50m} captures the neighborhood advective transport, profiles from LES_{20m} show a higher magnitude indicating that the LES_{50m} results are still grid-resolution dependent. This indicates that although hectometric LES manages to incorporate additional physics, the results are still grid-resolution dependent. A more detailed analysis of these fluxes is beyond the scope of the present analysis.

Fig. 16(e–f) further shows spatially averaged SHF profiles for the windy event. The profiles were averaged over a square area of approximately 6 km × 6 km in the center of Enschede. In both events, YSU produces a nearly linear decrease of SHF with height, consistent with its assumption of horizontal homogeneity, yielding entrainment fluxes of ∼25–50 $\mathrm{Wm^{-2}}$ near the PBL top. In contrast, LES exhibits non-standard (non-linear) vertical profiles in the urban boundary layer. These deviations from the near-linear profiles expected in idealized convective boundary layers arise because the assumptions underlying such profiles (horizontal homogeneity and statistical stationarity) are not satisfied

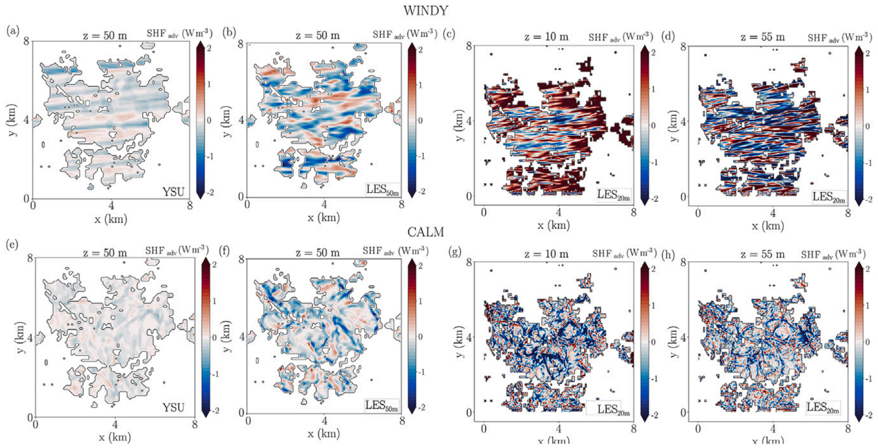

Fig. 15. Horizontal cross-section of horizontal advective SHF heating rate for (a,b,c,d) Windy event (on 2020-04-22 12:00 UTC) and (e,f,g,h) Calm event (on 2020-08-08 12:00 UTC), for YSU, $\mathrm{LES}_{50\mathrm{m}}$, and $\mathrm{LES}_{20\mathrm{m}}$, respectively.

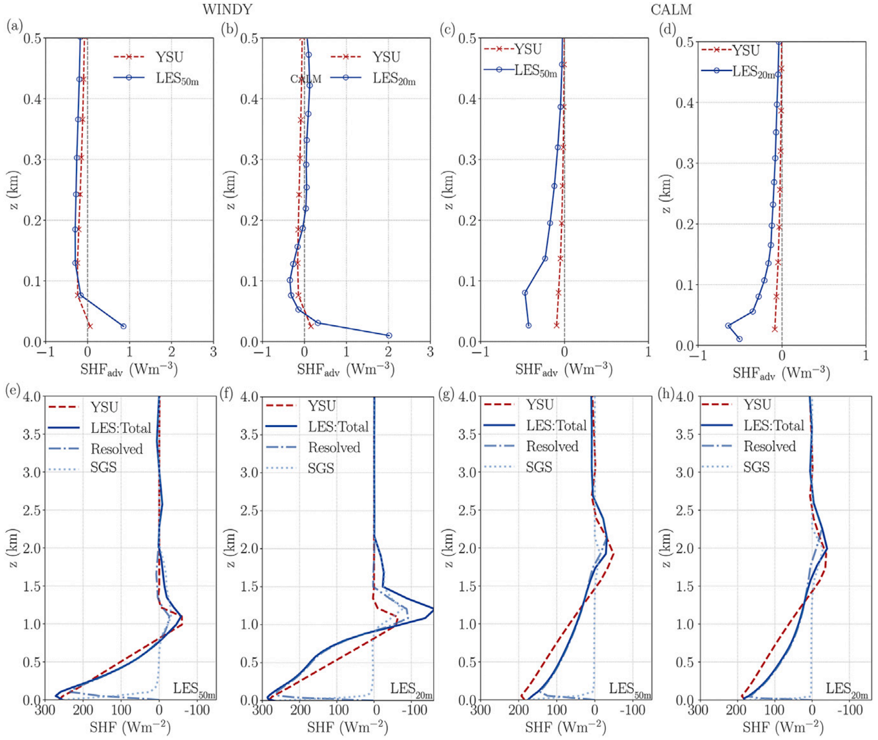

Fig. 16. Comparison of vertical profile of SHF_{adv} heating rate and SHF for YSU and LES models. (a,c,e,f) Windy event (on 2020-04-18 1200 UTC), and (b,d,g,h) Calm event (on 2020-08-08 1200 UTC), respectively.

in the present case. The urban surface is highly heterogeneous, and turbulent transport is dominated by spatially organized updrafts and downdrafts linked to surface contrasts. In addition, the boundary layer is evolving during the analysis period, as surface radiative forcing and urban heat storage change on timescales comparable to the 30-minute averaging window. Under such transient and heterogeneous conditions, spatial averaging does not necessarily recover the near-linear vertical flux profiles predicted for steady, homogeneous convective boundary layers.

This behavior is further illustrated by the higher-resolution $\mathrm{LES}_{20\mathrm{m}}$, which shows stronger entrainment flux at the top of the PBL for the windy event, while $\mathrm{LES}_{50\mathrm{m}}$ exhibits some resolution dependence. The comparison with $\mathrm{LES}_{20\mathrm{m}}$ indicates that resolution influences the magnitude and vertical distribution of turbulent fluxes, particularly during the Windy event. However, the overall non-linear profile shape persists across resolutions, suggesting that urban heterogeneity and coherent flow organization play a primary role. The partially resolved turbulent flux is further elaborated in Section 4.3. Similar behavior with non-standard profiles has been reported in hectometer-resolution LES over London by Lean et al. [36], with a slight near-surface increase in total flux also noted in hectometer and sub-hectometer simulations by Blunn et al. [2]. The partitioning between resolved and SGS fluxes in our study is also consistent with these studies [2,36].

During the calm event, convective cells redistribute heat vertically, producing large deviations from the linear profile. Although strongly convective boundary layers over homogeneous surfaces can exhibit

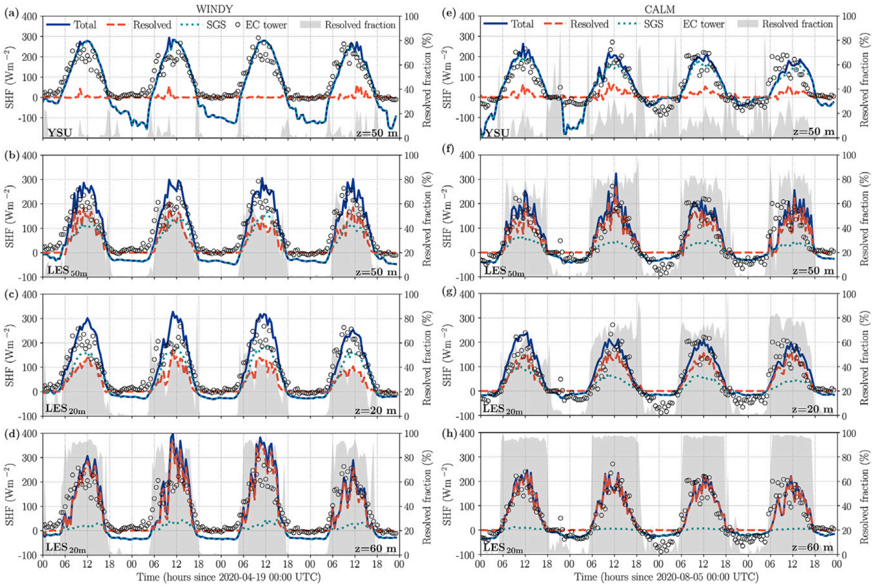

Fig. 17. Time series of resolved, SGS, and total turbulent SHF for (a, b, c, d) Windy event, (e,f,g,h) Calm event.

near-linear mean flux profiles after long averaging, the presence of spatially anchored convective cells and evolving surface forcing in the urban environment prevents the boundary layer from reaching such statistical equilibrium during the averaging window considered here. At the surface, fluxes are comparable for YSU and LES because they are constrained by the land surface model. However, as shown by the vertical profile of horizontal advection in LES, reorganization of fluxes above urban surfaces produces three-dimensional variability that is only marginally present in YSU. From Fig. 16(g) and (h), $\mathrm{LES}_{50\mathrm{m}}$ produces profiles that are very similar to those from $\mathrm{LES}_{20\mathrm{m}}$ under highly convective conditions, suggesting that hectometric resolution is sufficient to capture the dominant turbulent transport structures in buoyancy-driven regimes.

Finally, in LES for both windy and calm events, SGS turbulence dominates only very close to the urban surface, while most of the mixing within the urban boundary layer is explicitly resolved during daytime convective conditions. LES therefore provides a more explicit representation of the three-dimensional variability of turbulent transport above the surface layer, while we note that some quantitative aspects of the fluxes may remain resolution-dependent under certain conditions.

4.3. Resolved turbulence vs Modeled turbulence

As elaborated in the previous section, LES resolves large-scale convective rolls and cells, allowing a portion of the turbulent fluxes to be captured by these flow structures. This reduces WRF's dependence on parameterized turbulence, thereby minimizing model-related uncertainties in representing turbulent exchanges. It is therefore important to quantify the proportion of turbulence that is resolved by the model versus that which remains unresolved and must be parameterized through the SGS scheme. Fig. 17(a–d) presents the total, resolved, and SGS contributions to the surface SHF for the YSU, $\mathrm{LES}_{50\mathrm{m}}$, and $\mathrm{LES}_{20\mathrm{m}}$ during the Windy event. As shown previously, the YSU scheme does not resolve any turbulence structures, resulting in negligible resolved SHF and complete reliance on the SGS component. This highlights the model's strong dependence on the PBL scheme for representing turbulent processes. In contrast, Fig. 17(b) shows that in the $\mathrm{LES}_{50\mathrm{m}}$ simulation, nearly 50% of the turbulent SHF during daytime is resolved by the model, with the remaining 50% handled by the SGS scheme. However, during nighttime, when turbulent structures are smaller than the model's grid scale, both models rely entirely on SGS parameterization, and the resolved turbulence becomes negligible. This shows that at hectometric resolution $\mathrm{LES}_{50\mathrm{m}}$ although turbulence is resolved above the first atmospheric grid point, at 50-m height nearly 50% of the turbulence is modeled. However, with finer-scale $\mathrm{LES}_{20\mathrm{m}}$ at 60-m height nearly 80–90% more of the turbulence is resolved. Nonetheless, as the profiles shown in the previous section indicate, resolved turbulence increases above the first atmospheric level which will have implications on turbulence mixing in the PBL. It is worth mentioning here that we observe resolved turbulent fluxes not only with $\mathrm{LES}_{50\mathrm{m}}$ and $\mathrm{LES}_{20\mathrm{m}}$ but also with coarser resolution LES with $\Delta x, \Delta y = 500$ m. Comparison of turbulence structures and resolved scale fluxes with 500-m resolution LES is provided in Appendix C.

During the Calm event, as discussed in the previous section (Fig. 13(c)), convection generated a few turbulent structures in the YSU simulation. As a result, compared to the Windy event, a small amount of turbulence is resolved during the daytime, even with the YSU model (Fig. 17 c). While PBL schemes are typically designed under the assumption that all turbulence is sub-grid and must be parameterized, running these schemes at hectometric resolutions results in partial resolution of turbulent motions, even if limited. This overlap between resolved and parameterized turbulence may lead to double-counting of turbulent fluxes, introducing inconsistencies in the simulation of boundary layer processes. Our results show that YSU resolves nearly 20% of turbulence due to the partially developed structures presented in Fig. 13(e). In contrast, in the LES, the convective cells are approximately the size of the WRF grid, resulting in 80% of the daytime turbulence being explicitly resolved. Only a small portion remains to be represented by the sub-grid scale scheme Fig. 17(d). The difference in the percentage of resolved-scale turbulence between the windy and calm events arises from the dominance of shear during the windy event. Strong wind shear tends to break up large-scale turbulent structures into smaller eddies that fall below the model's grid resolution, resulting in a higher proportion of SGS flux in the windy event simulations.

It is important to note that nighttime SHF is entirely dependent on the PBL scheme in the YSU model and on the SGS turbulence scheme in LES. During nighttime, turbulent structures are typically smaller in scale [1] and therefore remain unresolved at hectometric resolution. Consequently, both YSU and LES rely on SGS parameterizations and we conclude that there is no benefit to performing hectometric LES under nighttime conditions.

5. Conclusions

This study compared WRF-LES at hectometric grid resolution with a traditional 1D PBL scheme (YSU) to evaluate whether LES achieves comparable performance for key urban climate variables, while also providing additional physics such as resolving turbulent structures, flux variability with height, the resolved - SGS turbulence partition, and horizontal advection. LES results showed broadly comparable agreement with observations to the YSU model in predicting near-surface variables, but with the added advantage of partially resolving turbulent motions during convective daytime conditions and revealing vertical variations in fluxes that remain hidden in 1D approaches. However, both approaches depend on parameterizations during nighttime conditions due to the coarse grid resolution.

Running WRF at 100 m horizontal and 50 m vertical resolution enabled the explicit resolution of large-scale turbulent eddies that are parameterized in mesoscale setups, during convectively forced portions of the diurnal cycle. Fluxes extracted at model levels corresponding to the measurement height highlight how LES provides more physically grounded representation of surface–atmosphere coupling. In particular, LES resolved convective rolls during the windy April event and convective cells during the calm August event during convective conditions. However, YSU failed to resolve any turbulent structures during the windy event and only partially developed turbulent structures during calm event which develop after a long fetch. However, the fact that YSU develops turbulent structures violates the underlying assumption of the PBL scheme that all turbulence is sub-grid scale. This leads to double-counting of turbulence and underlines the disadvantage of using PBL schemes at hectometric resolution.

LES reduced mean wind speed bias from 1.73 to 0.89 $\mathrm{ms^{-1}}$ during the windy event and from 0.47 to 0.02 $\mathrm{ms^{-1}}$ during the calm event. By extracting fluxes at appropriate model levels using WRFlux [16], we avoided inconsistencies inherent in the constant flux layer [61] assumption and showed that surface fluxes alone can misrepresent flux variability. Turbulence spectral analysis further confirmed that LES reproduces an inertial subrange, while absence of realistic spectra in YSU provided evidence of missing resolved motions. Therefore, at 50 m, LES fluxes displayed somewhat more realistic turbulent fluctuations similar to EC observations, whereas surface fluxes were overly smooth during day time. However, both LES and YSU were unable to reproduce near-surface fluxes during nighttime conditions.

Comparison of horizontal advective SHF revealed that LES captures substantially stronger lateral transport than YSU (up to 3–4 times larger) directly linked to the resolved turbulent structures (rolls and cells). However, it is worth mentioning that 100-m horizontal and 50-m vertical resolution is coarse and therefore these results are grid-dependent. These results are suggestive of increased lateral transport, which is further justified by the fine-resolution LES presented in our study. Vertical SHF profiles in LES deviate from the linear profile imposed by the 1D closure, reflecting the three-dimensional turbulent variability that the YSU scheme does not represent. During peak daytime turbulence, at 100-m horizontal and 50-m vertical resolution, LES resolved approximately 50% (windy case) to 80% (calm case) of the total flux at the first atmospheric level, reducing dependence on model assumptions and improving physical realism. However, both LES and YSU struggle during nocturnal stable conditions, where performance is sensitive to the SGS closure.

Overall, this study demonstrates the added value of hectometric WRF-LES for resolving realistic turbulent structures, capturing horizontal and vertical advective heat transport, and quantifying the balance between resolved and SGS fluxes. These capabilities are essential not only for urban heat flux studies but also for understanding plume dispersion, pedestrian-level thermal comfort, and the role of urban turbulence in convective initiation and extreme precipitation. Hectometric LES therefore provides a more physically grounded basis for advancing urban climate modeling in rapidly warming cities.

CRediT authorship contribution statement

Srinidhi Gadde: Writing – review & editing, Writing – original draft, Visualization, Validation, Methodology, Formal analysis, Data curation, Conceptualization. **Gert-Jan Steeneveld:** Writing – review & editing, Supervision. **Wim Timmermans:** Writing – review & editing, Supervision, Methodology, Funding acquisition.

Declaration of competing interest

The authors declare that they have no known competing financial interests or personal relationships that could have appeared to influence the work reported in this paper.

Acknowledgements

This work is supported by the 4TU program HERITAGE (HEat Robustness in Relation To AGEing cities), funded by the High Tech for a Sustainable Future (HTSF) program of 4TU, the federation of the four technical universities in the Netherlands. This work used the Dutch national e-infrastructure with the support of the SURF Cooperative using grant no. EINF-2023.042. We thank the three anonymous reviewers for their comments which helped improve the quality of the study.

Appendix A. Planetary boundary layer schemes used in the study

A.1. Yonsei university (YSU) PBL scheme

The YSU scheme is based on a ‘nonlocal-K’ approach [22] and includes counter-gradient fluxes to account for thermals and eddies of boundary-layer scale that transport heat and other properties based on bulk gradients which could be larger than, or of opposite sign when compared to local gradients. For the mixed layer ($z \leq h$, where h is height of the PBL), the turbulence diffusion equations for prognostic variable can be expressed by

$$\frac{\partial C}{\partial t} = -\frac{\partial}{\partial z}\overline{w'c'} = \frac{\partial}{\partial z}\left[K_c\left(\frac{\partial C}{\partial z} - \gamma_c\right) - \overline{w'c'}_h\left(\frac{z}{h}\right)^3\right], \tag{A.5}$$

where C represents the prognostic variable such as temperature, velocity, humidity etc., K_c is the eddy diffusivity, γ_c is the counter-gradient term which acts as a correction to the local gradient and adds the contribution of thermals and PBL scale eddies to the total flux, and $\overline{w'c'_h}$ is the flux at the inversion layer. $\overline{w'c'}_h\left(\frac{z}{h}\right)^3$ accounts for the entrainment flux at the top of the PBL. Due to the addition of nonlocal, counter-gradient term YSU model is well-suited for simulating convective boundary layers. More details about the YSU model can be found in Hong et al. [22]. It is amply clear from Eq. (A.5) that only 1D vertical turbulent exchange is assumed between the surface and the atmosphere.

A.2. Non-linear backscatter and anisotropy (NBA) model for SGS momentum flux and smagorinsky model for SGS heat flux

In LES, turbulence partially resolved and only the sub-grid scale turbulence is modeled. Total flux can therefore be represented as, $\tau_{ij} = \tau_{ij}^{resolved} + \tau_{ij}^{sgs}$. Resolved scale turbulence can be easily calculated based on time averages, using $\tau_{ij} = \overline{\widetilde{u_i u_j}} - \overline{\widetilde{u}_i \widetilde{u}_j}$, where the overbar represents time averaging, and tilde represents filtering based on the grid size. However, the SGS turbulence τ_{ij}^{sgs} needs to be modeled with an SGS model.

In our LES simulations we use the 3D NBA SGS model [41]. This model is based on a nonlinear constitutive relation that incorporates second-order terms, which account for both backscatter and normal stresses in the context of sheared homogeneous turbulence. The SGS stress within the NBA model can be expressed as a function of the strain rate, as shown below,

$$\begin{aligned}\tau_{ij}^{sgs} = -(C_s l)^2 \Big[2(2\tilde{S}_{mn}\tilde{S}_{mn})^{1/2}\tilde{S}_{ij} + C_1\left(\tilde{S}_{ik}\tilde{S}_{kj} - \frac{1}{3}\tilde{S}_{mn}\tilde{S}_{mn}\delta_{ij}\right) \\ + C_2(\tilde{S}_{ik}\tilde{R}_{kj} - \tilde{R}_{ik}\tilde{S}_{kj})\Big],\end{aligned} \tag{A.6}$$

where, $\tilde{S}_{ij} = \frac{1}{2}\left(\partial\tilde{u}_i/\partial x_j + \partial\tilde{u}_j/\partial x_i\right)$ is the resolved strain-rate tensor, $\tilde{R}_{ij} = \frac{1}{2}\left(\partial\tilde{u}_i/\partial x_j - \partial\tilde{u}_j/\partial x_i\right)$ is the resolved rotation-rate tensor, $C_s = \left[8\left(1+C_b\right)/27\pi^2\right]$, $C_1 = C_2 = 960^{1/2}C_b/7(1+C_b)S_k$, $S_k = 0.5$, and $C_b = 0.36$.

Model parameters in the NBA model depend only on one free parameter, the backscatter coefficient C_b. Based on Kosović [33] the backscatter coefficient is given a value of 0.36. In the limit of $C_b \rightarrow 0$, the NBA model reverts to linear eddy-viscosity Smagorinsky model. For detailed explanation of the NBA model we refer to Mirocha et al. [41] and Kosović [33].

Eq. (A.6) only provides the SGS momentum flux i.e., the eddy viscosity for SGS turbulent mixing, however the heat diffusion coefficient K_h is not modeled with the NBA model. Therefore, under the NBA model K_h is modeled using the Smagorinsky model, where similar to momentum flux, total heat flux is calculated as, $q_j = q_j^{resolved} + q_j^{sgs}$. Heat flux can be easily calculated based on time averages, using $q_j^{resolved} = \overline{\widetilde{u_j\theta}} - \overline{\tilde{u}_j}\,\overline{\tilde{\theta}}$, where overbar represents time averaging, the tilde represents filtering based on the grid size, and u_i represents the velocity.

The SGS heat flux is modeled as,

$$q_j^{sgs} = -K_h \frac{\partial\tilde{\theta}}{\partial x_j}, \tag{A.7}$$

$$K_h = \left((C_s l)^2\,(\tilde{S}_{ij}\tilde{S}_{ij})\right)/\mathrm{Pr}_t. \tag{A.8}$$

Here, K_h is the diffusion coefficient, $C_s = 0.16$ is the Smagorinsky coefficient. The length scale is calculated by $l = (\Delta x \Delta y \Delta z)^{1/3}$, Pr_t is the SGS turbulent Prandtl number. In Eq. (A.8), the Prandtl number is set based on the atmospheric stability quantified by the Brunt-Väisala frequency ($N^2 = \frac{g}{\theta}\frac{d\theta}{dz}$) with Pr_t values 0.33, 0.7, and 1.0 for unstable ($N^2 < 0$), neutral ($N^2 = 0$), and stable ($N^2 > 0$) conditions respectively [15,40].

Appendix B. Evaluation metrics

We use Root Mean Squared Error (RMSE) and Mean Bias Error (MBE) to quantify the average magnitude and direction of model errors, respectively. However, these metrics do not capture how well the model reproduces the observed variability and timing. Index of Agreement (IOA) is preferred over R^2 because it assesses both the accuracy and precision of the model, even when the observations have low variance unlike R^2, which can be misleading in such cases.

B.1. Root-mean-square error (RMSE)

The Root Mean Square Error (RMSE) measures the average magnitude of the errors between modeled and observed values. It is sensitive to large errors and is expressed in the same units as the variable being evaluated. RMSE is defined as:

$$\mathrm{RMSE} = \sqrt{\frac{1}{N}\sum_{i=1}^{N}(M_i - O_i)^2} \tag{B.9}$$

where M_i and O_i are the modeled and observed values, respectively, and N is the number of data points.

B.2. Mean bias error (MBE)

The Mean Bias Error (MBE) quantifies the average deviation between modeled and observed values, indicating whether the model systematically overestimates or underestimates the observations. A positive MBE implies overestimation, while a negative MBE implies underestimation. It is given by:

$$\mathrm{MBE} = \frac{1}{N}\sum_{i=1}^{N}(M_i - O_i) \tag{B.10}$$

B.3. Index of agreement (IOA)

The Index of Agreement (IOA) [69] is a dimensionless metric that quantifies the degree to which model predictions match the pattern and variability of observed values. It evaluates both the magnitude and direction of deviations relative to the mean of the observations, providing a normalized measure of model performance.

IOA is defined as,

$$\mathrm{IOA} = 1 - \frac{\sum_{i=1}^{N}|M_i - O_i|}{\sum_{i=1}^{N}\left(|M_i - \bar{O}| + |O_i - \bar{O}|\right)}. \tag{B.11}$$

IOA ranges from 0 to 1, where 1 indicates perfect agreement between modeled and observed values, and 0 represents complete disagreement. Low IOA values typically occur when the model's variability is out of phase with the observations—i.e., when the model consistently overestimates during low observed values and underestimates during high observed values, or vice versa.

Appendix C. Robustness of WRF-LES turbulent features at coarse horizontal resolution of 500 m

Fig. C.18 presents a comparison of the resolved and modeled fluxes at different horizontal resolutions and corresponding turbulent structures represented by vertical velocity. As can be seen in Fig. C.18(c) and (o) even at 500-m horizontal resolution turbulent structures are

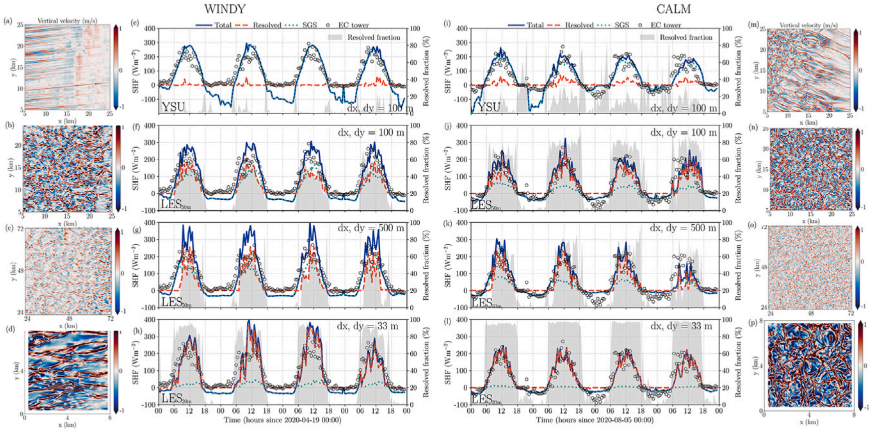

Fig. C.18. Time series of resolved, SGS, and total turbulent SHF for (a) Windy event, YSU, (b) Windy event, LES, (c) Calm event, YSU, and (d) Calm event, LES model. Shaded region and right axis represents the resolved flux fraction calculated as the ratio of resolved flux to the total flux.

resolved although the not at the same strength as 100-m horizontal resolution. Furthermore, the percentage of resolved flux is lower compared to LES with horizontal resolution of 100-m (Figs. C.18(g, k)) and 33-m (Figs. C.18(h, l)). However, both the resolved flux and turbulent structures indicate that the features are robust LES features and not just numerical artifacts. Fig. C.18 shows that at 500 m resolution the resolved sensible heat flux is reduced by up to 20% at the first atmospheric model level compared to the 100 m simulation. This result confirms the expected scale dependence of resolved turbulence, with finer horizontal resolution leading to a larger resolved flux fraction. Importantly, this comparison demonstrates that the enhanced resolved turbulence at 100 m resolution is not an artifact of a single grid choice but follows physically consistent resolution-dependent behavior.

Data availability

Data will be made available on request.

References

[1] R.J. Beare, M.K. Macvean, A.A. Holtslag, J. Cuxart, I. Esau, J.C. Golaz, et al., An intercomparison of large-eddy simulations of the stable boundary layer, Bound. Layer Meteorol. 118 (2006) 247–272, https://doi.org/10.1007/s10546-004-2820-6

[2] L.P. Blunn, R.S. Plant, O. Coceal, S.I. Bohnenstengel, H.W. Lean, J.F. Barlow, The influence of resolved convective motions on scalar dispersion in hectometric-scale numerical weather prediction models, Q. J. R. Meteorol. Soc. 150 (2024) 976–994, https://doi.org/10.1002/qj.4632

[3] CampbellScientific, CNR1: Kipp & Zonen, Net radiometer, 2025, https://www.campbellsci.com/cnr1 (Last Accessed: 2 February 2025).

[4] CampbellScientific, CSAT3: 3-D Sonic Anemometer, 2025, https://www.campbellsci.com/csat3 (Last Accessed: 2 February 2025).

[5] Y. Cao, T. Tao, Y. Shi, S. Cao, D. Zhou, W.L. Chen, Large-eddy simulation of separated turbulent flows over a three-dimensional hill using wrf and openfoam, J. Wind Eng. Ind. Aerodyn. 236 (2023) 105357, https://doi.org/10.1016/j.jweia.2023.105357

[6] CBS, Enschede Population, 2025. https://enschede.incijfers.nl/Jive/detailview?detailview_guid = 079ba730-9ac1-4bd7-a21f-cc87cf582986&geolevel = gemeente&geoitem = 153&period = m6y2025,m5y2025,m4y2025,m3y2025,m2y2025&title = Aantal%20inwoners&unittitle = %28maandcijfer%29.

[7] F. Chen, J. Dudhia, Coupling an advanced land surface–hydrology model with the penn state–ncar mm5 modeling system. part I: model implementation and sensitivity, Mon. Weather Rev. 129 (2001) 569–585, https://doi.org/10.1175/1520-0493(2001)129 < 0569:CAALSH > 2.0.CO;2.

[8] F. Chen, Z. Janjić, K. Mitchell, Impact of atmospheric surface-layer parameterizations in the new land-surface scheme of the ncep mesoscale eta model, Bound. Layer Meteorol. 85 (1997) 391–421, https://doi.org/10.1023/A:1000531001463

[9] F. Chen, H. Kusaka, R. Bornstein, J. Ching, C.S.B. Grimmond, S. Grossman-Clarke, et al., The integrated wrf/urban modelling system: development, evaluation, and applications to urban environmental problems, Int. J. Climatol. 31 (2011) 273–288, https://doi.org/10.1002/joc.2158

[10] J. Chen, N. Dong, Z. Liu, Y. Chen, M. Luo, H. Huang, Local temperature impact of urban heat mitigation strategy based on wrf integrating urban canopy parameters and local climate zones, Build. Environ. 267 (2025) 112257, https://doi.org/10.1016/j.buildenv.2024.112257

[11] J.W. Deardorff, Numerical investigation of neutral and unstable planetary boundary layers, J. Atmos. Sci. 29 (1972) 91–115, https://doi.org/10.1175/1520-0469(1972)029 < 0091:NIONAU > 2.0.CO;2

[12] M. Demuzere, C. He, A. Martilli, A. Zonato, Technical documentation for the hybrid 100-m global land cover dataset with Local Climate Zonesfor WRF, 2023, https://doi.org/10.5281/zenodo.7670792

[13] T. Foken, M. Göockede, M. Mauder, L. Mahrt, B. Amiro, W. Munger, Post-field data quality control. In: Handbook of Micrometeorology: A Guide for Surface Flux Measurement and Analysis, Springer, 2004, pp. 181–208.

[14] A. Forster, C. Augros, V. Masson, Urban influence on convective precipitation in the paris region: hectometric ensemble simulations in a case study, Q. J. R. Meteorol. Soc. 150 (2024) 3028–3051, https://doi.org/10.1002/qj.4749

[15] S.N. Gadde, A. Stieren, R.J. Stevens, Large-eddy simulations of stratified atmospheric boundary layers: comparison of different subgrid models, Bound. Layer Meteorol. 178 (2021) 363–382, https://doi.org/10.1007/s10546-020-00570-5

[16] M. Göbel, S. Serafin, M.W. Rotach, Numerically consistent budgets of potential temperature, momentum, and moisture in cartesian coordinates: application to the wrf model, Geosci. Model Dev. 15 (2022) 669–681, https://doi.org/10.5194/gmd-15-669-2022

[17] R.L. Grossman, An analysis of vertical velocity spectra obtained in the bomex fair-weather, trade-wind boundary layer, Bound. Layer Meteorol. 23 (1982) 323–357, https://doi.org/10.1007/BF00121120

[18] K.E. Hanley, A.I. Barrett, H.W. Lean, Simulating the 20 May 2013 Moore, Oklahoma tornado with a 100-metre grid-length nwp model, Atmos. Sci. Lett. 17 (2016) 453–461, https://doi.org/10.1002/asl.678

[19] C. Heaviside, X.M. Cai, S. Vardoulakis, The effects of horizontal advection on the urban heat island in Birmingham and the West Midlands, United Kingdom during a heatwave, Q. J. R. Meteorol. Soc. 141 (2015) 1429–1441, https://doi.org/10.1002/qj.2452

[20] H. Hersbach, B. Bell, P. Berrisford, S. Hirahara, A. Horányi, J. Muñoz-Sabater, et al., The era5 global reanalysis, Q. J. R. Meteorol. Soc. 146 (2020) 1999–2049, https://doi.org/10.1002/qj.3803

[21] A.A.M. Holtslag, B.A. Boville, Local versus nonlocal boundary-layer diffusion in a global climate model, J. Clim. 6 (1993) 1825–1842, https://doi.org/10.1175/1520-0442(1993)006 < 1825:LVNBLD > 2.0.CO;2

[22] S.Y. Hong, Y.H. Noh, J. Dudhia, A new vertical diffusion package with an explicit treatment of entrainment processes, Mon. Weather Rev. 134 (2006) 2318–2341, https://doi.org/10.1175/MWR3199.1

[23] X.M. Hu, J.W. Nielsen-Gammon, F. Zhang, Evaluation of three planetary boundary layer schemes in the wrf model, J. Appl. Meteorol. Climatol. 49 (2010) 1831–1844, https://doi.org/10.1175/2010JAMC2432.1

[24] M. Huang, Z. Gao, S. Miao, F. Chen, Sensitivity of urban boundary layer simulation to urban canopy models and pbl schemes in Beijing, Meteorol. Atmos. Phys. 131 (2019) 1235–1248, https://doi.org/10.1007/s00703-018-0634-1

[25] M.J. Iacono, J.S. Delamere, E.J. Mlawer, M.W. Shephard, S.A. Clough, W.D. Collins, Radiative forcing by long-lived greenhouse gases: calculations with the aer radiative transfer models, J. Geophys. Res. Atmos. 113 (2008), https://doi.org/10.1029/2008JD009944

[26] P.A. Jiménez, J. Dudhia, J.F. González-Rouco, J. Navarro, J.P. Montávez, E. García-Bustamante, A revised scheme for the wrf surface layer formulation, Mon. Weather Rev. 140 (2012) 898–918, https://doi.org/10.1175/MWR-D-11-00056.1

[27] M.Y. Joshi, J. Teller, Assessing urban heat island mitigation potential of realistic roof greening across local climate zones: a highly-resolved weather research and forecasting model study, Sci. Total Environ. (2024), https://doi.org/10.1016/j.scitotenv.2024.173728

[28] T.W. Juliano, B. Kosović, P.A. Jiménez, M. Eghdami, S.E. Haupt, A. Martilli, “Gray zone” simulations using a three-dimensional planetary boundary layer parameterization in the weather research and forecasting model, Mon. Weather Rev. 150 (2022) 1585–1619, https://doi.org/10.1175/MWR-D-21-0164.1

[29] J.C. Kaimal, J.J. Finnigan, Atmospheric Boundary Layer Flows: Their Structure and Measurement, Oxford University Press, 1994.

[30] S. Khanna, J.G. Brasseur, Three-dimensional buoyancy-and shear-induced local structure of the atmospheric boundary layer, J. Atmos. Sci. 55 (1998) 710–743, https://doi.org/10.1175/1520-0469(1998)055 < 0710:TDBASI > 2.0.CO;2

[31] KNMI, Knmi heatwave definition, 2025, https://www.knmi.nl/kennis-en-datacentrum/uitleg/hittegolf (Last Accessed: 7 Feb 2025).

[32] KNMI, Knmi cloudcover measurements, 2025, https://www.knmi.nl/kennis-en-datacentrum/achtergrond/licht-op-wolken-toepassing-van-de-lidar-in-de-meteorologie (Last Accessed: 7 Feb 2025).

[33] B. Kosović, Subgrid-scale modelling for the large-eddy simulation of high-reynolds-number boundary layers, J. Fluid Mech. 336 (1997) 151–182, https://doi.org/10.1017/S0022112096004697

[34] B. Kosović, P.J. Munoz, T. Juliano, A. Martilli, M. Eghdami, A. Barros, et al., Three-dimensional planetary boundary layer parameterization for high-resolution mesoscale simulations, in: Journal of Physics: Conference Series, IOP Publishing, 2020, https://doi.org/10.1088/1742-6596/1452/1/012080. p. 012080.

[35] H. Kusaka, H. Kondo, Y. Kikegawa, F. Kimura, A simple single-layer urban canopy model for atmospheric models: comparison with multi-layer and slab models, Bound. Layer Meteorol. 101 (2001) 329–358, https://doi.org/10.1023/A:1019207923078

[36] H.W. Lean, J.F. Barlow, C.H. Halios, The impact of spin-up and resolution on the representation of a clear convective boundary layer over london in order 100 m grid-length versions of the met office unified model, Q. J. R. Meteorol. Soc. 145 (2019) 1674–1689, https://doi.org/10.1002/qj.3519

[37] H.W. Lean, N.E. Theeuwes, M. Baldauf, J. Barkmeijer, G. Bessardon, L. Blunn, et al., The hectometric modelling challenge: gaps in the current state of the art and ways forward towards the implementation of 100-m scale weather and climate models, Q. J. R. Meteorol. Soc. 150 (2024) 4671–4708, https://doi.org/10.1002/qj.4858

[38] D. Li, E. Bou-Zeid, M. Oppenheimer, The effectiveness of cool and green roofs as urban heat island mitigation strategies, Environ. Res. Lett. 9 (2014) 055002, https://doi.org/10.1088/1748-9326/9/5/055002

[39] F. Lindberg, C.S.B. Grimmond, A. Gabey, B. Huang, C.W. Kent, T. Sun, et al., Urban multi-scale environmental predictor (umep): an integrated tool for city-based climate services, Environ. Model. Softw. 99 (2018) 70–87, https://doi.org/10.1016/j.envsoft.2017.09.020

[40] P.J. Mason, A.R. Brown, On subgrid models and filter operations in large eddy simulations, J. Atmos. Sci. 56 (1999) 2101–2114, https://doi.org/10.1175/1520-0469(1999)056 < 2101:OSMAFO > 2.0.CO;2

[41] J. Mirocha, J. Lundquist, B. Kosović, Implementation of a nonlinear subfilter turbulence stress model for large-eddy simulation in the advanced research wrf model, Mon. Weather Rev. 138 (2010) 4212–4228, https://doi.org/10.1175/2010MWR3286.1

[42] E.J. Mlawer, S.J. Taubman, P.D. Brown, M.J. Iacono, S.A. Clough, Radiative transfer for inhomogeneous atmospheres: Rrtm, a validated correlated-k model for the longwave, J. Geophys. Res. Atmos. 102 (1997) 16663–16682, https://doi.org/10.1029/97JD00237

[43] C.H. Moeng, P.P. Sullivan, A comparison of shear-and buoyancy-driven planetary boundary layer flows, J. Atmos. Sci. 51 (1994) 999–1022, https://doi.org/10.1175/1520-0469(1994)051 < 0999:ACOSAB > 2.0.CO;2

[44] C.H. Moeng, A large-eddy-simulation model for the study of planetary boundary-layer turbulence, J. Atmos. Sci. 41 (1984) 2052–2062, https://doi.org/10.1175/1520-0469(1984)041 < 2052:ALESMF > 2.0.CO;2

[45] D. Muñoz-Esparza, B. Kosović, J. Mirocha, J. van Beeck, Bridging the transition from mesoscale to microscale turbulence in numerical weather prediction models, Bound. Layer Meteorol. 153 (2014) 409–440, https://doi.org/10.1007/s10546-014-9956-9

[46] M.R. Raupach, R.A. Antonia, S. Rajagopalan, Rough-wall turbulent boundary layers, ASME. Appl. Mech. Rev. 44 (1991) 1–25, https://doi.org/10.1115/1.3119492

[47] I. Ribeiro, A. Martilli, M. Falls, A. Zonato, G. Villalba, Highly resolved wrf-bep/bem simulations over barcelona urban area with lcz, Atmos. Res. 248 (2021) 105220, https://doi.org/10.1016/j.atmosres.2020.105220

[48] R. Ronda, G. Steeneveld, B. Heusinkveld, J. Attema, A. Holtslag, Urban finescale forecasting reveals weather conditions with unprecedented detail, Bull. Am. Meteorol. Soc. 98 (2017) 2675–2688, https://doi.org/10.1175/BAMS-D-16-0297.1

[49] J.A. Ruiz-Arias, J. Dudhia, F.J. Santos-Alamillos, D. Pozo-Vázquez, Surface clear-sky shortwave radiative closure intercomparisons in the weather research and forecasting model, J. Geophys. Res. Atmos. 118 (2013) 9901–9913, https://doi.org/10.1002/jgrd.50778

[50] F. Salamanca, A. Martilli, M. Tewari, F. Chen, A study of the urban boundary layer using different urban parameterizations and high-resolution urban canopy parameters with wrf, J. Appl. Meteorol. Climatol. 50 (2011) 1107–1128, https://doi.org/10.1175/2010JAMC2538.1

[51] F. Salamanca, Y. Zhang, M. Barlage, F. Chen, A. Mahalov, S. Miao, Evaluation of the wrf-urban modeling system coupled to noah and noah-mp land surface models over a semiarid urban environment, J. Geophys. Res. Atmos. 123 (2018) 2387–2408, https://doi.org/10.1002/2018JD028377

[52] S.T. Salesky, M. Chamecki, E. Bou-Zeid, On the nature of the transition between roll and cellular organization in the convective boundary layer, Bound. Layer Meteorol. 163 (2017) 41–68, https://doi.org/10.1007/s10546-016-0220-3

[53] D.P. Sarmiento, K.J. Davis, A. Deng, T. Lauvaux, A. Brewer, M. Hardesty, A comprehensive assessment of land surface-atmosphere interactions in a wrf/urban modeling system for indianapolis, Elem. Sci. Anth. 5 (2017) 23, https://doi.org/10.1525/elementa.132

[54] A. Sharma, P. Conry, H. Fernando, A.F. Hamlet, J. Hellmann, F. Chen, Green and cool roofs to mitigate urban heat island effects in the Chicago metropolitan area: evaluation with a regional climate model, Environ. Res. Lett. 11 (2016) 064004, https://doi.org/10.1088/1748-9326/11/6/064004

[55] Y. Shi, T. Tao, H. Wu, Y.R. Chen, Z. Han, D. Zhou, et al., Assessment of turbulence model effects on wrf-les of separated turbulent flows past a 3d hill, J. Wind Eng. Ind. Aerodyn. 254 (2024) 105910, https://doi.org/10.1016/j.jweia.2024.105910

[56] G. Simó, J. Cuxart, M.A. Jiménez, D. Martínez-Villagrasa, R. Picos, A. López-Grifol, et al., Observed atmospheric and surface variability on heterogeneous terrain at the hectometer scale and related advective transports, J. Geophys. Res. Atmos. 124 (2019) 9407–9422, https://doi.org/10.1029/2018JD030164

[57] W.C. Skamarock, J.B. Klemp, J. Dudhia, D.O. Gill, D.M. Barker, M.G. Duda, et al., A description of the advanced research wrf version 3, NCAR Tech. Note 475 (2008) 10–5065, https://doi.org/10.5065/D68S4MVH

[58] J. Smagorinsky, General circulation experiments with the primitive equations: I. the basic experiment, Mon. Weather Rev. 91 (1963) 99–164, https://doi.org/10.1175/1520-0493(1963)091<0099:GCEWTP>2.3.CO;2

[59] I.D. Stewart, T.R. Oke, Local climate zones for urban temperature studies, Bull. Am. Meteorol. Soc. 93 (2012) 1879–1900, https://doi.org/10.1175/BAMS-D-11-00019.1

[60] R.B. Stull, An Introduction to Boundary Layer Meteorology, vol. 13, Springer Science & Business Media, 1988, https://doi.org/10.1007/978-94-009-3027-8

[61] R.B. Stull, An Introduction to Boundary Layer Meteorology, vol. 13, Springer Science & Business Media, 2012.

[62] P.P. Sullivan, E.G. Patton, The effect of mesh resolution on convective boundary layer statistics and structures generated by large-eddy simulation, J. Atmos. Sci. 68 (2011) 2395–2415, https://doi.org/10.1175/JAS-D-10-05010.1

[63] G. Thompson, R.M. Rasmussen, K. Manning, Explicit forecasts of winter precipitation using an improved bulk microphysics scheme. part I: description and sensitivity analysis, Mon. Weather Rev. 132 (2004) 519–542, https://doi.org/10.1175/1520-0493(2004)132<0519:EFOWPU>2.0.CO;2

[64] J.V. Tito, A.P.D. Oliveira, M.P. Sánchez, A. Fornaro, Evaluation of nine planetary boundary layer turbulence parameterization schemes of the weather research and forecasting model applied to simulate planetary boundary layer surface properties in the metropolitan region of São Paulo megacity, Brazil, Atmosphere 15 (2024) 785, https://doi.org/10.3390/atmos15070785

[65] Vaisala, Vaisala Weather Transmistter WXT520, 2012, https://www.vaisala.com/sites/default/files/documents/M210906EN-C.pdf (Last Accessed: 2 Feb 2025).

[66] S. Vosper, E. Carter, H. Lean, A. Lock, P. Clark, S. Webster, High resolution modelling of valley cold pools, Atmos. Sci. Lett. 14 (2013) 193–199, https://doi.org/10.1002/asl2.439

[67] T.M. Weckwerth, T.W. Horst, J.W. Wilson, An observational study of the evolution of horizontal convective rolls, Mon. Weather Rev. 127 (1999) 2160–2179, https://doi.org/10.1175/1520-0493(1999)127<2160:AOSOTE>2.0.CO;2

[68] D.J. Wiersema, K.A. Lundquist, J.D. Mirocha, F. Katopodes Chow, Evaluation of turbulence and dispersion in multiscale atmospheric simulations over complex urban terrain during the joint urban 2003 field campaign, Mon. Weather Rev. 150 (2022) 3195–3209, https://doi.org/10.1175/MWR-D-22-0056.1

[69] C.J. Willmott, S.G. Ackleson, R.E. Davis, J.J. Feddema, K.M. Klink, D.R. Legates, et al., Statistics for the evaluation and comparison of models, J. Geophys. Res. Oceans 90 (1985) 8995–9005, https://doi.org/10.1029/JC090iC05p08995

[70] J.C. Wyngaard, Toward numerical modeling in the "terra incognita.", J. Atmos. Sci. 61 (2004) 1816–1826, https://doi.org/10.1175/1520-0469(2004)061<1816:TNMITT>2.0.CO;2

[71] B. Xie, J.C. Fung, A. Chan, A. Lau, Evaluation of nonlocal and local planetary boundary layer schemes in the wrf model, J. Geophys. Res. Atmos. 117 (2012), https://doi.org/10.1029/2011JD017080

[72] X. Zhang, G.J. Steeneveld, D. Zhou, R.J. Ronda, C. Duan, S. Koopmans, et al., Modelling urban meteorology with increasing refinements for the complex morphology of a typical chinese city (Xi'an), Build. Environ. 182 (2020) 107109, https://doi.org/10.1016/j.buildenv.2020.107109

[73] D. Zhu, R. Ooka, Wrf-based scenario experiment research on urban heat island: a review, Urban Clim. 49 (2023) 101512, https://doi.org/10.1016/j.uclim.2023.101512

[74] D. Zhu, X. Zhou, W. Cheng, Water effects on urban heat islands in summer using wrf-ucm with gridded urban canopy parameters—a case study of Wuhan, Build. Environ. 225 (2022) 109528, https://doi.org/10.1016/j.buildenv.2022.109528